Journal of Computational Physics 371 (2018) 92–110

Contents lists available at ScienceDirect

Journal of Computational Physics

www.elsevier.com/locate/jcp

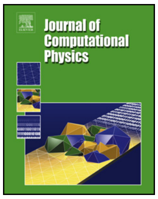

A differential variational approach for handling fluid–solid interaction problems via smoothed particle hydrodynamics

H. Mazhar [a], A. Pazouki [b], M. Rakhsha [a], P. Jayakumar [c], D. Negrut [a],*

[a] Department of Mechanical Engineering, University of Wisconsin–Madison, Madison, WI 53706-1572, USA
[b] Department of Mechanical Engineering, California State University, Los Angeles, CA 90032, USA
[c] U.S. Army Tank Automotive Research Development and Engineering Center, Warren, MI 48397-5000, USA

ARTICLE INFO

Article history:
Received 20 March 2017
Received in revised form 3 February 2018
Accepted 7 May 2018
Available online 15 May 2018

Keywords:
Fluid–solid interaction
Smoothed Particle Hydrodynamics
Incompressible flow
Kinematic constraints
Differential variational approach
Friction and contact

ABSTRACT

The fluid–solid interaction (FSI) problem is customarily solved by starting with the fluid dynamics component. One chooses an established computational fluid dynamics (CFD) method and subsequently embeds the solid phase dynamics within the CFD solution leading to either a monolithic or a staggered/co-simulated solution. The approach discussed here takes the opposite tack. We start with a differential variational framework to handle the solid phase; i.e., the multi-body dynamics problem in the presence of contact, friction, and bilateral kinematic constraints. The dynamics of the fluid phase, which is captured via smoothed particle hydrodynamics (SPH), is subsequently embedded into this framework in which the incompressibility attribute of the flow is enforced via kinematic constraint equations that involve SPH particles. The resulting monolithic FSI solution methodology relies on a half-implicit symplectic time integration method that uses a matrix-free iterative approach to solve a cone constrained quadratic optimization problem at each time step. This problem yields the contact forces, friction forces, boundary condition Lagrange multipliers, fluid–solid coupling terms, and bilateral constraint Lagrange multipliers. The solution of the optimization problem represents the computationally taxing component of the method. Large integration time steps, tight enforcement of incompressibility, a unified approach for handling the fluid and solid phases, and linear scaling are listed as the attractive attributes of the proposed method. The numerical experiments reported include three validation studies (incompressibility, dam break, and sloshing), a scaling analysis, and a tracked vehicle fording simulation.

1. Preliminaries

We are interested in the dynamics of articulated mechanical systems operating while totally or partially immersed in a fluid. Examples include particles in suspension; fully saturated soils; submersible vehicles, which contain rigid and/or flexible components; or other collections of objects whose mutual interaction, while governed by friction and contact forces, is modulated by the presence of the fluid phase via two-way coupling. For the purpose of introducing the modeling and numerical solution framework promoted herein, we concentrate on the fluid – rigid-body two way coupling. The case of

---

* Corresponding author.
E-mail addresses: mazhar@wisc.edu (H. Mazhar), apazouk@calstatela.edu (A. Pazouki), rakhsha@wisc.edu (M. Rakhsha), paramsothy.jayakumar.civ@mail.mil (P. Jayakumar), negrut@wisc.edu (D. Negrut).

https://doi.org/10.1016/j.jcp.2018.05.013

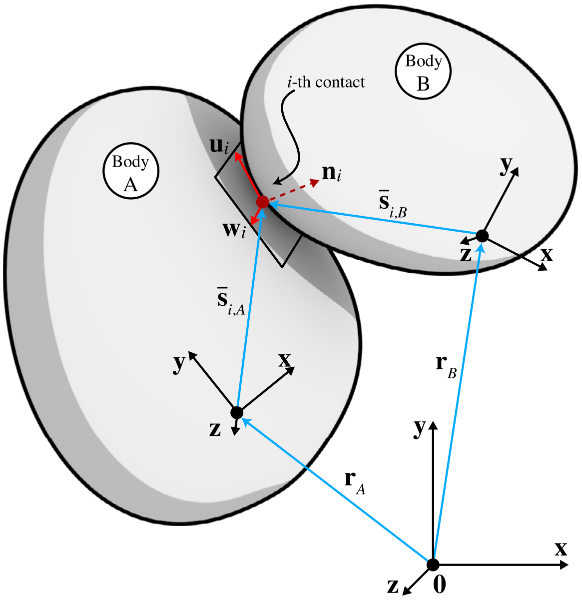

Fig. 1. The ith contact between two bodies A and B.

flexible/compliant bodies interacting with fluid, which can be similarly treated albeit using a more cumbersome notation, is discussed in [1].

2. The dynamics of the solid phase

2.1. The equations of motion

The time-evolution of a collection of n_b rigid bodies interacting through friction and contact is described herein using Cartesian coordinates associated with each body j, where $1 \le j \le n_b$. The array of generalized coordinates $\mathbf{q} = [\mathbf{r}_1^T, \boldsymbol{\epsilon}_1^T, \dots, \mathbf{r}_{n_b}^T, \boldsymbol{\epsilon}_{n_b}^T]^T \in \mathbb{R}^{7n_b}$, and its time derivative $\dot{\mathbf{q}} = [\dot{\mathbf{r}}_1^T, \dot{\boldsymbol{\epsilon}}_1^T, \dots, \dot{\mathbf{r}}_{n_b}^T, \dot{\boldsymbol{\epsilon}}_{n_b}^T]^T \in \mathbb{R}^{7n_b}$, are used to represent the state of the system, where for body j, $\mathbf{r}_j$ and $\boldsymbol{\epsilon}_j$ are the absolute position of the center of mass and the body orientation Euler parameters, respectively. For the body-centroidal and principal reference frame, $\boldsymbol{\epsilon}_j$ are defined with respect to a global and inertial reference frame. The time derivative $\dot{\boldsymbol{\epsilon}}_j$ of the Euler parameters can be replaced with a different set of unknowns; i.e., the angular velocity in local coordinates $\bar{\boldsymbol{\omega}}_j$, which ushers in the velocity $\mathbf{v} = [\dot{\mathbf{r}}_1^T, \bar{\boldsymbol{\omega}}_1^T, \dots, \dot{\mathbf{r}}_{n_b}^T, \bar{\boldsymbol{\omega}}_{n_b}^T]^T$. Using this notation, the time evolution of a system of bodies that interact with each other through contact, friction, external forces, and bilateral constraints is the solution of a set of differential algebraic equations, see for instance [2],

$$\dot{\mathbf{q}} = \mathbf{L}^s(\mathbf{q})\mathbf{v} \tag{1a}$$

$$\mathbf{M}^s\dot{\mathbf{v}} = \mathbf{f}^s(t,\mathbf{q},\mathbf{v}) + \mathbf{G}^s\hat{\lambda}^s + \sum_{i\in\mathcal{A}(\mathbf{q},\delta)} \underbrace{\left(\widehat{\gamma}^s_{i,n}\,\mathbf{D}^s_{i,n} + \widehat{\gamma}^s_{i,u}\,\mathbf{D}^s_{i,u} + \widehat{\gamma}^s_{i,w}\,\mathbf{D}^s_{i,w}\right)}_{i\text{th frictional contact force}} \tag{1b}$$

$$\mathbf{0} = \mathbf{g}^s(\mathbf{q},t) \tag{1c}$$

$$i \in \mathcal{A}^s(\mathbf{q}(t)) \;:\; \begin{cases} 0 \le C^s_i(\mathbf{q}) \perp \widehat{\gamma}^s_{i,n} \ge 0 \\ \left(\widehat{\gamma}^s_{i,u}, \widehat{\gamma}^s_{i,w}\right) = \underset{\sqrt{\gamma_u^2+\gamma_w^2}\le\mu_i^s\widehat{\gamma}^s_{i,n}}{\operatorname{argmin}} \quad \mathbf{v}^T\cdot\left(\gamma_u\,\mathbf{D}^s_{i,u} + \gamma_w\,\mathbf{D}^s_{i,w}\right) \end{cases} \tag{1d}$$

The differential equations in Eq. (1a) relate the time derivative of the generalized positions $\mathbf{q}$ and velocities $\mathbf{v}$ through a linear transformation defined by a block diagonal matrix $\mathbf{L}^s(\mathbf{q})$ [3]. The force balance equation in Eq. (1b) ties together the inertial force that employs the constant generalized mass matrix $\mathbf{M}^s \in \mathbb{R}^{6n_b\times 6n_b}$, the external force $\mathbf{f}^s(t,\mathbf{q},\mathbf{v})$, the bilateral constraint force $\mathbf{G}^s(t,\mathbf{q})\hat{\lambda}^s$, and the frictional contact forces. The superscript "s" emphasizes that these are solid-phase specific quantities. The bilateral constraint force, which is impressed by the set of bilateral kinematic constraints, see Eq. (1c), restricts the relative motion of solid bodies via the Lagrange multiplier $\hat{\lambda}^s$. In practical applications, the bilateral constraints in Eq. (1c) are associated with the presence of mechanical joints. For instance, a vehicle suspension is attached to the chassis using revolute joints, spherical joints, etc., which define the expression of the projection operator $\mathbf{G}^s$.

The summation for frictional contact forces, which are emphasized in Eq. (1b) using an under-brace, runs over all the contacts in the active set $\mathcal{A}^s(\mathbf{q}, \delta)$; i.e., the collection of N_K active contacts associated with pairs of bodies which given a generalized position $\mathbf{q}$ are within a relative distance less than or equal to a user prescribed threshold $\delta \geq 0$. A contact scenario is shown in Fig. 1. For two bodies A and B in contact, $0 \leq A < B \leq n_b$, let $\bar{\mathbf{s}}_{i,A}$ and $\bar{\mathbf{s}}_{i,B}$ be the location of the contact point with respect to the reference frame of body A and B, respectively. Since we are concerned with rigid bodies, $A \neq B$; the ground is assigned $A = 0$, and no self-contact is assumed. If the bodies in contact are defined by smooth boundaries, let $\mathbf{n}_i$ be the unit vector denoting the contact normal direction, and $\mathbf{u}_i$ and $\mathbf{w}_i$ be two unit vectors that span the contact plane at the point of contact. By convention, $\mathbf{n}_i$ points towards the interior of B, and $\{\mathbf{n}_i, \mathbf{u}_i, \mathbf{w}_i\}$ form a right-hand reference frame. The contact force, $\mathbf{F}_i$, associated with contact i can be decomposed into normal and tangential/frictional components, $\mathbf{F}_{i,N}$ and $\mathbf{F}_{i,T}$, respectively, where $\mathbf{F}_{i,N} = \hat{\gamma}^s_{i,n}\mathbf{n}_i$ and $\mathbf{F}_{i,T} = \hat{\gamma}^s_{i,u}\mathbf{u}_i + \hat{\gamma}^s_{i,w}\mathbf{w}_i$. As far as body B is concerned, $\hat{\gamma}^s_{i,n} \geq 0$.

Finally, the first row in Eq. (1d) poses a complementarity condition: the product of the gap function and the normal force, while both nonnegative quantities, is always zero. Specifically, if there is a gap between the bodies; i.e., $0 \leq C^s_i(\mathbf{q})$, then the normal force $\hat{\gamma}^s_{i,n}$ is zero. Conversely, if the gap is zero, the normal force is nonnegative. The friction force is tied to the value of the normal force via the Coulomb friction model. Using a *maximum dissipation principle*, see, for instance [4], the Coulomb friction force is obtained for each contact $i \in \mathcal{A}^s(\mathbf{q}, \delta)$ as the solution of the optimization problem in Eq. (1d). Its solution provides the components $\hat{\gamma}^s_{i,u}$ and $\hat{\gamma}^s_{i,w}$ of the friction force given a friction coefficient μ_i, the velocity $\mathbf{v}$, and the normal force at the contact point $\hat{\gamma}^s_{i,n}$. A transformation matrix $\mathbf{A}_i = [\mathbf{n}_i, \mathbf{u}_i, \mathbf{w}_i] \in \mathbb{R}^{3\times 3}$ is used for contact i to express the frictional contact force in the global frame. The projection matrix $\mathbf{D}^s_i \in \mathbb{R}^{6n_b\times 3}$,

$$\mathbf{D}^s_i = [\mathbf{0}_{3\times 3}, \ldots, \mathbf{0}_{3\times 3}, -\mathbf{A}_i^T, \mathbf{A}_i^T\mathbf{A}_A\tilde{\bar{\mathbf{s}}}_{i,A}, \mathbf{0}_{3\times 3}, \ldots, \mathbf{0}_{3\times 3}, \mathbf{A}_i^T, -\mathbf{A}_i^T\mathbf{A}_B\tilde{\bar{\mathbf{s}}}_{i,B}, \mathbf{0}_{3\times 3}, \ldots, \mathbf{0}_{3\times 3}]^T, \tag{2}$$

is used to express the generalized frictional contact force. Here, $\mathbf{A}_A$ and $\mathbf{A}_B$ are the body A and B rotational matrices, respectively; a tilde over a vector denotes its skew-symmetric matrix [3]; and, in terms of notation, $\mathbf{D}^s_i \equiv [\mathbf{D}^s_{i,n}, \mathbf{D}^s_{i,u}, \mathbf{D}^s_{i,u}]$ for the columns of the projection operator $\mathbf{D}^s_i$ [2].

2.2. Elements of the numerical solution

The mixed differential variational inequality problem in Eq. (1) is discretized to yield the mathematical program with complementarity and equality constraints in Eq. (3). The discretization is based on a symplectic half-implicit Euler method [5] used to advance the state of the system from time $t^{(l)}$ to $t^{(l+1)}$ with a step size Δt. The instantaneous Lagrange multipliers are scaled to become constraint reaction impulses: $\lambda \equiv \Delta t\, \hat{\lambda}$ for bilateral constraints; and, $\gamma \equiv \Delta t\, \hat{\gamma}_\alpha$, $\alpha \in \{n, u, w\}$, for the normal (n) and two tangential friction (u and w) forces. This discretization yields a first-order scheme [6]:

$$\overbrace{\mathbf{q}^{(l+1)}}^{\text{Generalized positions}} = \mathbf{q}^{(l)} + \overbrace{\Delta t}^{\text{Step size}}\ \underbrace{\mathbf{L}^s(\mathbf{q}^{(l)})}_{\text{Velocity transformation matrix}}\mathbf{v}^{(l+1)} \tag{3a}$$

$$\mathbf{M}^s(\overbrace{\mathbf{v}^{(l+1)}}^{\text{Gen. speeds}} - \mathbf{v}^{(l)}) = \underbrace{\Delta t\, \mathbf{f}^s(t^{(l)}, \mathbf{q}^{(l)}, \mathbf{v}^{(l)})}_{\text{Applied impulse}} + \overbrace{\mathbf{G}^s\lambda^{s,(l+1)}}^{\text{Bilat. constr. impulse}} + \underbrace{\mathbf{D}^s\gamma^{s,(l+1)}}_{\text{Frictional contact reaction impulses}} \tag{3b}$$

$$0 = \underbrace{\frac{1}{\Delta t}\mathbf{g}^s(\mathbf{q}^{(l)}, t^{(l)})}_{\text{Stabilization term}} + \mathbf{G}^{s,T}\mathbf{v}^{(l+1)} + \mathbf{g}^s_t \tag{3c}$$

$$i \in \mathcal{A}^{s,(l)}\ :\ \begin{cases} 0 \leq \overbrace{\dfrac{1}{\Delta t}C^s_i(\mathbf{q}^{(l)})}^{\text{Stabilization term}} + \mathbf{D}^{s,T}_{i,n}\mathbf{v}^{(l+1)} \overbrace{-\mu^s_i\sqrt{(\mathbf{D}^{s,T}_{i,u}\cdot\mathbf{v}^{(l+1)})^2 + (\mathbf{D}^{s,T}_{i,w}\cdot\mathbf{v}^{(l+1)})^2}}^{\text{Relaxation term}} \perp \gamma^{s,(l+1)}_{i,n} \geq 0 \\ \left(\gamma^{s,(l+1)}_{i,u}, \gamma^{s,(l+1)}_{i,w}\right) = \underset{\sqrt{\gamma_u^2+\gamma_w^2}\leq\mu^s_i\gamma^{s,(l+1)}_{i,n}}{\operatorname{argmin}} \quad \mathbf{v}^T\cdot\left(\gamma_u\,\mathbf{D}^s_{i,u} + \gamma_w\,\mathbf{D}^s_{i,w}\right), \end{cases} \tag{3d}$$

where $\mathbf{D}^s \equiv [\mathbf{D}^s_1\ \mathbf{D}^s_2 \ldots \mathbf{D}^s_{N_K}] \in \mathbb{R}^{6n_b\times 3N_K}$, and $\mathbf{g}^s_t \equiv \frac{\partial\mathbf{g}^s}{\partial t}$ is the partial derivative of the bilateral constraints with respect to time. For the unilateral; i.e., non-penetration or inequality, constraints the friction cone $\mathcal{K}_i$ associated with contact event $i \in \mathcal{A}^{s,(l)}$ is defined as $\mathcal{K}_i \equiv \{[x,\ y,\ z]^T \in \mathbb{R}^3 :\quad 0 \leq x \text{ and } \mu_i x - \sqrt{y^2+z^2} \geq 0\}$. The polar cone $\mathcal{K}^\circ_i$ associated with the friction cone $\mathcal{K}_i$ is defined as $\mathcal{K}^\circ_i \equiv \{[a,\ b,\ c]^T \in \mathbb{R}^3 : ax + by + cz \leq 0\ \forall\,[x,\ y,\ z]^T \in \mathcal{K}_i\}$. For equality constraints, the cone $\mathcal{B}_j \equiv \mathbb{R}$ and the polar cone $\mathcal{B}^\circ_j \equiv \{y :\ x\cdot y \leq 0\ \forall\, x \in \mathcal{B}_j\}$. Note that this polar cone set has only one element: $\mathcal{B}^\circ_j = \{0\}$. Next, define two quantities: $\mathbf{d}_i \equiv [\frac{1}{\Delta t}C^{s,(l)}_i,\ 0,\ 0]^T + \mathbf{D}^{s,T}_i(\mathbf{v}^{(l)} + \Delta t\,\mathbf{M}^{s,-1}\,\mathbf{f}^{s,(l)}) \in \mathbb{R}^3$ and $b_j \equiv \frac{1}{\Delta t}\,\mathbf{g}^{s,(l)}_j + \frac{\partial\mathbf{g}^{s,(l)}_j}{\partial t} + \mathbf{G}^{s,T}_j(\mathbf{v}^{(l)} + \Delta t\,\mathbf{M}^{s,-1}\,\mathbf{f}^{s,(l)}) \in \mathbb{R}$, already available at $t^{(l)}$. Define $\mathbf{P}_s \equiv \left[\mathbf{D}^{s,(l)}_i\ \ \mathbf{G}^{s,(l)}\right] \in \mathbb{R}^{6n_b\times(3N_K+N_B)}$, and

$$\boldsymbol{\nu}_s^{(l+1)} \equiv \begin{bmatrix} \gamma^{s,(l+1)} \\ \lambda^{s,(l+1)} \end{bmatrix} \in \mathbb{R}^{3N_K+N_B} \ , \quad \mathbf{p}_s \equiv \left[\mathbf{d}_1^{s,T}, \ldots, \mathbf{d}_{N_K}^{s,T}, b_1^s, \ldots, b_{N_B}^s \right]^T \in \mathbb{R}^{3N_K+N_B} .$$

The discretized problem can be posed as a Cone Complementarity Problem (CCP): find $\boldsymbol{\nu}_s^{(l+1)}$ such that

$$\mathcal{C}_{s,k} \ni \boldsymbol{\nu}_{s,k}^{(l+1)} \quad \perp \quad -(\mathbf{p}_s + \mathbf{N}_s \boldsymbol{\nu}_s^{(l+1)})_k \in \mathcal{C}_{s,k}^{\circ} \ , \tag{4}$$

where $\mathbf{N}_s \equiv \mathbf{P}_s^T \mathbf{M}^{s,-1} \mathbf{P}_s$, $\mathcal{C}_s \equiv \mathcal{K}_{s,1} \oplus \ldots \oplus \mathcal{K}_{s,N_K} \oplus \mathcal{B}_1 \oplus \ldots \oplus \mathcal{B}_{N_B}$, and $\mathcal{C}_s^{\circ} \equiv \mathcal{K}_{s,1}^{\circ} \oplus \ldots \oplus \mathcal{K}_{s,N_K}^{\circ} \oplus \mathcal{B}_1^{\circ} \oplus \ldots \oplus \mathcal{B}_{N_B}^{\circ}$. As shown in [2], this CCP represents the first order optimality condition [7] for the convex quadratic optimization problem with conic constraints

$$\begin{aligned} \boldsymbol{\nu}_s^{(l+1)} &= \min_{\boldsymbol{\nu}} \frac{1}{2} \boldsymbol{\nu}^T \mathbf{N}_s \boldsymbol{\nu} + \mathbf{p}_s^T \boldsymbol{\nu} \\ &\quad \text{subject to } \boldsymbol{\nu}_{s,k} \in \mathcal{C}_{s,k} \ . \end{aligned} \tag{5}$$

Once available, $\boldsymbol{\nu}_s^{(l+1)}$ is used in Eq. (3b) to obtain the velocities $\mathbf{v}^{(l+1)}$, which are then used in Eq. (3a) to get the generalized positions $\mathbf{q}^{(l+1)}$. This completes the $t^{(l+1)}$ state update.

The key steps of the solution methodology are as follows: the unilateral and equality kinematic constraints are imposed at the velocity level. Any constraint drift at the position level is remedied via the terms labeled "Stabilization term" in Eqs. (3c) and (3d). Introducing the "Relaxation term" in Eq. (3d) changes the nature of the numerical problem from a nonlinear complementarity problem into a CCP. The latter is equivalently posed as a quadratic optimization problem with conic constraints. The optimization problem is convex, which ensures a global solution. Moreover, the solution is unique in velocities and therefore positions [8].

3. Handling the dynamics of the fluid phase

3.1. The equations of motion

The time evolution of the fluid phase is the solution of a set of partial differential equations that capture the mass and momentum balance, see Eq. (6). Under the assumption of dealing with Newtonian incompressible fluids, the mass and momentum balance equations are stated as [9,10]

$$\dot{\rho} = -\rho \nabla \cdot \mathbf{v}^f \tag{6a}$$

$$\dot{\mathbf{v}}^f = -\frac{1}{\rho} \nabla p + \frac{\mu}{\rho} \nabla^2 \mathbf{v}^f + \hat{\mathbf{f}}^f \ , \tag{6b}$$

where μ is the fluid viscosity, ρ the fluid density, $\mathbf{v}^f$ and p are the flow velocity and pressure, respectively, and $\hat{\mathbf{f}}^f$ is the fluid external body force. Mass conservation can be posed as one of the following conditions:

$$\nabla \cdot \mathbf{v}^f = 0 \tag{7a}$$

$$\dot{\rho} = 0 \ , \tag{7b}$$

the latter stating that density is constant along particle paths. Herein, we assume that the density is time and material point independent, and, with ρ_0 constant, we use everywhere

$$\rho = \rho_0 \ , \tag{7c}$$

in lieu of the differential counterpart in Eq. (7b).

3.2. Elements of the numerical solution

For the discretization of the Navier–Stokes equations we draw on the Smoothed Particle Hydrodynamics (SPH) methodology [11,12], a meshless method that dovetails well with the Lagrangian perspective of the solid phase. In SPH, the fluid domain is discretized via moving particles. A particle a has mass m_a associated with the representative volume $d\mathbb{V}$, carries all of the essential field properties, and influences its neighborhood via a smoothing function W that uses a characteristic smoothing length h to establish a compact support domain. Any field property is evaluated as a weighted sum of contributions made by the particles in the vicinity of a location of interest [13].

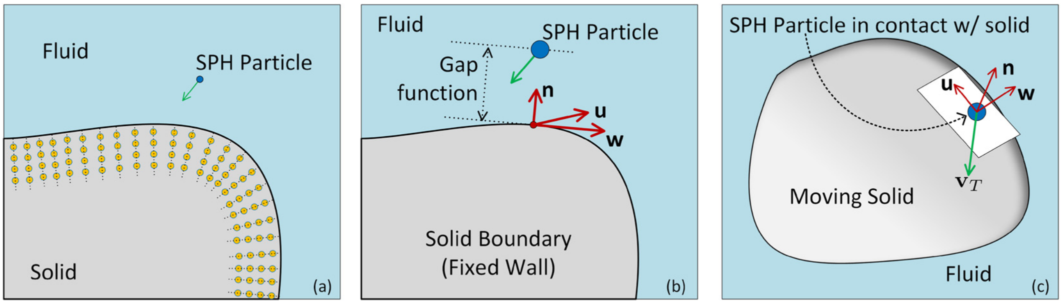

Fig. 2. (a): Boundary conditions and/or fluid–solid coupling imposed via ghost SPH particles deployed in a buffer volume on and near the surface of the solid. The ghost particles are rigidly attached to solid; (b) Boundary conditions enforced in CFSPH via non-penetration unilateral constraints posed as complementarity conditions; (c) Moving solid interacting with SPH particle – the particle is shown moving in tangent plane with velocity $\mathbf{v}_T$.

3.2.1. *The classical, weakly compressible SPH (WCSPH) approach*

In this classical approach, the density is usually obtained using [14]

$$\rho_i = \sum_j m_j W_{ij} \qquad \text{or,} \tag{8a}$$

$$\frac{d\rho_i}{dt} = \rho_i \sum_j \frac{m_j}{\rho_j} \mathbf{v}^f_{ij} \cdot \nabla_i W_{ij} \,, \tag{8b}$$

where a subscript i indexes a quantity associated with particle i, and the superscript f is used in conjunction with the fluid phase. Moreover, $\mathbf{x}_{ij} = \mathbf{x}_i - \mathbf{x}_j$, $\mathbf{v}^f_{ij} = \mathbf{v}^f_i - \mathbf{v}^f_j$, $W_{ij} = W(\mathbf{x}_{ij}, h)$, and ∇_i is the gradient with respect to the $\mathbf{x}_i$ position of SPH particle i. Each approach in Eq. (8) has its own merits and drawbacks, and an implementation might alternatively use both in conjunction with a density re-initialization method, see, for instance, [15].

The momentum equation Eq. (6b) is discretized at an arbitrary location $\mathbf{x}_i$ as [16,17]

$$\frac{d\mathbf{v}^f_i}{dt} = -\sum_j m_j \left[\left(\frac{p_i}{{\rho_i}^2} + \frac{p_j}{{\rho_j}^2} \right) \nabla_i W_{ij} - \frac{(\mu_i + \mu_j)\mathbf{x}_{ij} \cdot \nabla_i W_{ij}}{\bar{\rho}^2_{ij}(x^2_{ij} + \varepsilon h^2)} \mathbf{v}^f_{ij} \right] + \hat{\mathbf{f}}^f_i \,, \tag{9}$$

where ε is a regularization coefficient and $\bar{\rho}_{ij}$ is the average density of particles i and j. In WCSPH, the pressure is related to the density through the Murnaghan–Tait equation of state

$$p = \left(c^2_s \rho_0 / \gamma \right) \left\{ (\rho/\rho_0)^\gamma - 1 \right\} \,, \tag{10}$$

where c_s is the numerical speed of sound and γ adjusts the stiffness of the pressure–density relationship.

Succinctly, at each time step t_n, the solution is advanced as follows. First, the value of ρ is used in the state equation to compute p. The density and pressure are used in Eqs. (8b) and (9) to calculate the particle's density and velocity rates of change; alternatively, Eq. (8a) could be considered in place of Eq. (8b) to calculate density directly. A second order explicit mid-point scheme [18] updates the particle's position via $\frac{d\mathbf{x}_i}{dt} = \mathbf{v}^f_i$. In the so-called extended SPH approach [19], the particle velocity that entered the right hand side of Eqs. (8b) as well as the definition of $\frac{d\mathbf{x}_i}{dt}$ is replaced with $\hat{\mathbf{v}}^f_i$

$$\hat{\mathbf{v}}^f_i = \mathbf{v}^f_i - \frac{1}{2} \sum_j m_j \frac{\mathbf{v}^f_{ij}}{\bar{\rho}_{ij}} W_{ij}. \tag{11}$$

The fluid–solid coupling Several methods have been proposed in literature for fixed or moving solid boundary in WCSPH, see, for instance, [17,20–22]. In the past, we employed the "dummy particle" approach of [23,24], in which Boundary Condition Enforcing (BCE) particles were distributed in/on the rigid [25] or flexible [26] bodies. The "dummy particle" approach is shown in Fig. 2(a) using four layers of BCE particles, which are constrained to move with the solid body. At the fluid–solid interface, via Eqs. (8) and (9), each BCE particle captures an interaction force due to the presence of nearby fluid particles. The velocity and pressure of a BCE particle that enters those equations can be estimated in two different ways. The particle velocity can be replaced by the local velocity of the moving, solid-phase, boundary; the pressure requires a projection from the fluid domain [24]. Alternatively, in the so called "momentum-balance" solution, the velocity of each BCE particle is calculated so that when combined with the fluid contribution it results in the assigned wall velocity; additionally, the BCE particle pressure is obtained from a force balance at the boundary [21]. The momentum-balance approach performs better in imposing the no-slip condition, particularly when the external body force is significant [27]. All these approaches are straightforward to implement, yet incompressibility is only weakly enforced and integration step sizes are small.

3.2.2. The proposed, constraint-based approach

The WCSPH solution requires an equation of state for closure. The higher the speed of sound c_s and/or exponent γ, the closer the numerical solution comes to the abstraction of incompressible fluid. However, this renders the problem numerically stiff, which places a tight upper bound on the integration step size. To solve this conundrum, an implicit or semi-implicit approach can dismiss the equation of state and determine the pressure by enforcing the solenoidal nature of the velocity field. In this context, by using the mass balance equation as a constraint on the dynamics of the fluid phase, the pressure trades its thermodynamic meaning as sensitivity of the internal energy with respect to the volume element for one in which the pressure gradient represents the force field that enforces the incompressibility condition. A fractional step approach reminiscent of the methodology proposed for classical CFD in [28] has been outlined in conjunction with SPH in [29]. Enforcing the incompressibility via a pressure projection step then calls for the solution of an elliptical Poisson problem. This adds to the computational cost per numerical integration step, yet allows for larger time steps. One drawback of this methodology is that enforcing the divergence free condition in velocities only enforces that the time derivative of the density stays constant. This, however, does not protect against drift in constraint satisfaction. Several corrections to address drift have been proposed in [29]. The first and more common approach remains rooted into a velocity projection via the solution of a Poisson problem but yields methods that improve (i) the boundary condition enforcement in the Poisson problem [30,31]; and/or (ii) the splitting that handles the viscosity in time-explicit [32,23,33] or -implicit [34] fashions. A second approach that enforces incompressibility operates directly on the expression of the density. Indeed, the condition $\rho_i = \rho_0$ becomes a holonomic kinematic constraint that leads to the presence of reaction forces whose net effect is that of adjusting SPH particle trajectories to maintain density invariance. This approach has been proposed in [35] and revisited in [36,37]. Enforcing incompressibility via a kinematic constraint is attractive since (a) it prevents drift in enforcing the incompressibility condition, and (b) it does not pose additional challenges for enforcing the boundary conditions in the Poisson problem. The latter issue is particularly daunting given that handling boundary conditions in SPH is not straightforward and remains a topic of ongoing research. Typically, one resorts to adding dummy [23] or ghost particles [38] to capture the fluid–solid interaction. The process is nontrivial for moving solid bodies or when handling walls with corners and nooks [24].

The approach proposed herein enforces the incompressibility via holonomic kinematic constraints. As shown shortly, the discretized equations of motion for the fluid component assume a form that is *identical* to that of the discretized equations of motion that govern the time evolution of a constrained rigid, multi-body system. This opens the door to numerical solutions that handle the FSI problem in one framework. To this end, we formulate the following holonomic kinematic constraint in conjunction with each SPH particle: the density ρ_i at the location of particle i should assume at all times the target density ρ_0; i.e.,

$$\mathbf{g}_i^f \equiv \frac{\rho_i - \rho_0}{\rho_0} = 0\,, \tag{12}$$

where $\mathbf{g}^f(\mathbf{x}) = \mathbf{0}_{N_F}$ is the collection of incompressibility constraints.

The starting point in setting up the constrained-fluid SPH (CFSPH) approach is the observation that when expressing a derivative $\frac{\partial A}{\partial x}$ in SPH, it is recommended to use the identity

$$\frac{\partial A}{\partial x} = \frac{1}{\Psi}\left[\frac{\partial(\Psi A)}{\partial x} - A\frac{\partial \Psi}{\partial x}\right],$$

where Ψ is a sufficiently differentiable function [14]. Setting $\Psi = 1$ in conjunction with the mass balance equation leads to Eq. (8b) of WCSPH. In CFSPH, the choice $\Psi = \rho$ leads to

$$\dot{\mathbf{g}}_i^f = \frac{d}{dt}\left(\frac{\rho_i}{\rho_0} - 1\right) = \sum_j \frac{m_j}{\rho_0}\mathbf{v}_i^f \cdot \nabla_i W_{ij} - \sum_j \frac{m_j}{\rho_0}\mathbf{v}_j^f \cdot \nabla_i W_{ij} = 0\,. \tag{13}$$

In anticipation of the numerical solution method used in CFSPH, the generalized force projection operators for the density constraint associated with particle i are evaluated as

$$\mathbf{G}_{ii}^f = \frac{1}{\rho_0}\sum_{k\neq i} m_k \nabla W_{ik} \in \mathbb{R}^{1\times 3} \qquad \text{and} \qquad \mathbf{G}_{ij}^f = -\frac{m_j}{\rho_0}\nabla W_{ij} \in \mathbb{R}^{1\times 3} \quad \text{for } i \neq j\,,\ 1 \leq j \leq N_F\,. \tag{14}$$

Each density constraint contributes one row in the kinematic constraint Jacobian matrix, the latter being of size $N_F \times 3N_F$, where N_F is the number of SPH fluid particles. Each row i has three values in columns $3i$, $3i+1$, and $3i+2$; and three values for each neighboring SPH particle j; i.e., a particle which is sufficiently close to particle i to impact the value of the density at the location of the latter. The sparsity pattern of the Jacobian changes in time, but the fill-in stays roughly the same since over time each SPH particle is expected to have a relatively constant number of neighbor particles.

An insufficient number of fluid particles associated with the typical SPH discretization leads to poor approximations of the density near free-surface boundaries or walls. This particle deficiency is addressed as follows: for SPH particles close to a free surface or wall, the density in Eq. (12) assumes the expression [39]

$$\rho_i = \frac{\sum_j^N m_j W_{ij}}{\sum_j^N \frac{m_j}{\rho_j} W_{ij}} \, .$$

CFSPH treatment of boundaries Boundary conditions (BC) associated with fixed boundaries (walls) are posed as non-penetration, unilateral, constraints just like when handling contact for the solid phase. Referring to Fig. 2(b) and (c), if the gap between an SPH particle and a wall is greater than zero, the normal force imposed by the wall upon particle is zero; vice-versa, if the gap is less than or equal to zero, a nonzero normal force $\widehat{\gamma}_n^{bc}$ enforces the non-penetration condition. The BC yields a complementarity equation that captures a unilateral kinematic constraint. Friction between the solid boundaries and the fluid models both energy losses at the fluid–solid interface as well as no-slip conditions. These modeling decisions made in conjunction with the SPH spatial discretization of the Navier–Stokes equations lead to the following differential variational inequality problem [1]:

$$\dot{\mathbf{x}} = \mathbf{v}^f \tag{15a}$$

$$\dot{\mathbf{v}}^f = \underbrace{\mathbf{f}^f\left(t, \mathbf{x}, \mathbf{v}^f\right)}_{\text{Body, Pressure, Visc. force}} + \overbrace{\mathbf{G}^f \widehat{\lambda}^f}^{\text{Incompres. enforcing}} + \overbrace{\mathbf{D}^{bc} \widehat{\gamma}^{bc}}^{\text{Boundary coupling}} \tag{15b}$$

$$\underbrace{\mathbf{g}^f(\mathbf{x}, t)}_{\text{Density constraints (incompres. enforcement)}} = \mathbf{0} \tag{15c}$$

$$k \in \mathcal{A}^{bc}(\mathbf{x}(t), \delta_{bc}) \ : \ \begin{cases} 0 \le \widehat{\gamma}_{k,n}^{bc} \perp \overbrace{C_k^{bc}}^{\text{Fluid–solid nonpenetration condition}}(\mathbf{x}) \ge 0 \\ \\ \left(\widehat{\gamma}_{k,u}^{bc}, \widehat{\gamma}_{k,w}^{bc}\right) = \underset{\sqrt{\gamma_u^2 + \gamma_w^2} \le \mu_k^{bc} \widehat{\gamma}_{k,n}^{bc}}{\operatorname{argmin}} \ \overbrace{\mathbf{v}_k^T \left(\gamma_u \mathbf{u}_k^{bc} + \gamma_w \mathbf{w}_k^{bc}\right)}^{\text{F–S coupling dissipation energy}} \ , \end{cases} \tag{15d}$$

where $\mathbf{x} = [\mathbf{x}_1^T, \ldots, \mathbf{x}_{N_F}^T]^T \in \mathbb{R}^{3N_F}$, $\mathbf{f}^f\left(t, \mathbf{x}, \mathbf{v}^f\right)$ is defined as the right side of Eq. (9), $\mathbf{G}^f \in \mathbb{R}^{3N_F \times N_F}$ is defined via Eq. (14), and $\widehat{\lambda}^f \in \mathbb{R}^{N_F}$ is the associated Lagrange multiplier. The BC enforcing is captured in Eq. (15d) where for a $\mathbf{x}(t)$ distribution of the SPH particles, $\mathcal{A}^{bc}(\mathbf{x}(t), \delta_{bc})$ denotes the collection of contact events triggered by SPH particles that are within a threshold distance $\delta_{bc} \ge 0$ from a wall. Note that the same SPH particle, in theory, can be involved in more than one contact event. When within δ_{bc} from a wall, a fluid particle j is treated as a rigid sphere that, depending on its velocity $\mathbf{v}_j^f$, might inelastically collide within the current time-step Δt with a wall and subsequently mutually interact via frictional contact. This unilateral constraint looks like the one encountered when handling rigid bodies but with one caveat: the fluid particle only has translational degrees of freedom, which simplifies the constraint. Defining $\mathbf{A}_k^{bc} \equiv [\mathbf{n}_k^{bc}, \mathbf{u}_k^{bc}, \mathbf{w}_k^{bc}] \in \mathbb{R}^{3\times 3}$, the projection operator $\mathbf{D}_k^{bc}$, which for a contact event k projects the frictional contact force $\widehat{\gamma}^{bc}$ upon the SPH particle j, assumes the expression

$$\mathbf{D}_k^{bc} = \left[\mathbf{0}_{3\times 3}, \ldots, \mathbf{0}_{3\times 3}, -\mathbf{A}_k^{bc,T}, \mathbf{0}_{3\times 3}, \ldots, \mathbf{0}_{3\times 3}\right]^T \equiv [\mathbf{D}_{k,n}^{bc} \ \mathbf{D}_{k,u}^{bc} \ \mathbf{D}_{k,w}^{bc}] \in \mathbb{R}^{3N_F \times 3} \, .$$

This is the analog of the projector operator in Eq. (2). The projection operator $\mathbf{D}^{bc} \equiv [\mathbf{D}_1^{bc} \ldots \mathbf{D}_{N_{bc}}^{bc}] \in \mathbb{R}^{3N_F \times 3N_{bc}}$ and associated Lagrange multiplier $\widehat{\gamma}^{bc} \in \mathbb{R}^{3N_{bc}}$ come into play to enforce non-penetration conditions between fluid particles and boundaries/walls. Here $N_{bc} = |\mathcal{A}^{bc}(\mathbf{x}(t), \mathbf{q}(t), \delta_{bc})|$ is the number of contact events between SPH particles and boundaries. It changes at each time step and is determined via a proximity computation stage that parallels the collision detection task for the solid phase. Finally, in Eq. (15d), the maximum dissipation principle ties the power dissipated to the value of the friction force $\gamma_u \mathbf{u}_k^{bc} + \gamma_w \mathbf{w}_k^{bc}$ and the relative velocity $\mathbf{v}_k$ between the SPH particle and the solid. A zero friction coefficient μ_k^{bc} indicates no wettability, with larger values increasingly arresting the slip of the SPH particles.

CFSPH time discretization The differential variational inequality in Eq. (15) is discretized via the half-implicit symplectic Euler scheme used for the solid component, see Eq. (3):

$$\mathbf{x}^{(l+1)} = \mathbf{x}^{(l)} + \Delta t\, \mathbf{v}^{f,(l+1)} \tag{16a}$$

$$\overbrace{\mathbf{v}^{f,(l+1)}}^{\text{Generalized speeds}} - \mathbf{v}^{f,(l)} = \Delta t\, \mathbf{f}^{f,(l)}(t, \mathbf{x}, \mathbf{v}^{f}) + \overbrace{\mathbf{G}^{f} \lambda^{f,(l+1)}}^{\text{Density Impulse}} + \underbrace{\mathbf{D}^{bc} \gamma^{bc,(l+1)}}_{\text{Boundary Impulse}} \tag{16b}$$

$$0 = \underbrace{\frac{1}{\Delta t} \mathbf{g}^{f}(\mathbf{x}^{(l)})}_{\text{Density Stabilization}} + \mathbf{G}^{f,T} \mathbf{v}^{f,(l+1)} \tag{16c}$$

$$k \in \mathcal{A}^{bc,(l)} \;:\; \begin{cases} 0 \le \underbrace{\dfrac{C_k^{bc}(\mathbf{x}^{(l)})}{\Delta t}}_{\text{Contact Stabilization}} + \mathbf{D}_{k,n}^{bc,T} \mathbf{v}^{f,(l+1)} \overbrace{- \mu_k^{bc} \sqrt{\left(\mathbf{D}_{k,u}^{bc,T} \mathbf{v}^{f,(l+1)}\right)^2 + \left(\mathbf{D}_{k,w}^{bc,T} \mathbf{v}^{f,(l+1)}\right)^2}}^{\text{Relaxation Term}} \perp \gamma_{k,n}^{bc,(l+1)} \ge 0 \\ \left(\gamma_{k,u}^{bc,(l+1)}, \gamma_{k,w}^{bc,(l+1)}\right) = \underset{\sqrt{\gamma_u^2 + \gamma_w^2} \le \mu_k^{bc} \gamma_{k,n}^{bc,(l+1)}}{\operatorname{argmin}} \mathbf{v}^{f,(l+1),T} \left(\gamma_u \mathbf{D}_{k,u}^{bc} + \gamma_w \mathbf{D}_{k,w}^{bc}\right) \end{cases} \tag{16d}$$

In Eq. (16), any quantity without a superscript or with superscript (l) is evaluated at time $t^{(l)}$; any quantity evaluated at $t^{(l+1)}$ displays a $(l+1)$ superscript. Equation (16b) is the discretized version of Eq. (15b) upon multiplication by the step size Δt. Therefore, unknowns are now impulses rather than Lagrange multipliers; i.e., $\lambda^f \equiv \Delta t\, \hat{\lambda}^f$ and $\gamma^{bc} \equiv \Delta t\, \hat{\gamma}^{bc}$. Equation (16c) is a first order Taylor series truncation of Eq. (15c), when the latter is enforced in the configuration at the end of the time step; i.e., $\mathbf{x}^{(l+1)}$. The "*Density Stabilization*" term $\frac{1}{\Delta t}\mathbf{g}^f(\mathbf{x}^{(l)})$ compensates for violations in satisfying the density kinematic constraint in Eq. (15c), an approach that follows in the steps of the constraint stabilization proposed in [40]. In doing so, we don't enforce the density constraint at the position level but rather constrain the velocity of the SPH particles by imposing a velocity-level equation that accounts at $t^{(l+1)}$ for any density drift manifest at $t^{(l)}$. The same "stabilization" approach is embraced to enforce the BC non-penetration condition. Moreover, for a fluid–solid interaction event $k \in \mathcal{A}^{bc,(l)}$, the Taylor expansion of the gap function evaluated at $t^{(l+1)}$ is: (a) truncated to first order; and, (b) relaxed via a "*Relaxation Term*" to transform the discretized equations of motion in Eq. (16) into a CCP, as done for the solid body dynamics discretization in Eq. (3d). Let

$$\begin{aligned} \mathbf{d}_i^f &\equiv [\frac{1}{\Delta t} C_i^{bc,(l)},\ 0,\ 0]^T + \mathbf{D}_i^{bc,(l),T}(\mathbf{v}^{f,(l)} + \Delta t\, \mathbf{f}^{f,(l)}) \in \mathbb{R}^3 \\ b_j^f &\equiv \frac{1}{\Delta t}\mathbf{g}_j^{f,(l)} + \mathbf{G}_j^{f,(l),T}(\mathbf{v}^{f,(l)} + \Delta t\, \mathbf{f}^{f,(l)}) \in \mathbb{R}\,. \end{aligned}$$

All quantities that enter the computation of $\mathbf{d}_i^f$ and b_j^f are computed based on information available at the beginning of the step; i.e., at $t^{(l)}$. Likewise, let

$$\begin{aligned} \mathbf{P}_f &\equiv \begin{bmatrix} \mathbf{D}^{bc,(l)} & \mathbf{G}^{f,(l)} \end{bmatrix} \in \mathbb{R}^{3N_F \times (3N_{bc}+N_F)}\,, \\ \boldsymbol{\nu}_f^{(l+1)} &\equiv \begin{bmatrix} \gamma^{f,(l+1)} \\ \lambda^{f,(l+1)} \end{bmatrix} \in \mathbb{R}^{3N_{bc}+N_F} \quad \text{and,} \\ \mathbf{p}_f &\equiv \begin{bmatrix} \mathbf{d}_1^{f,T}, \ldots, \mathbf{d}_{N_K}^{f,T}, b_1^f, \ldots, b_{N_B}^f \end{bmatrix}^T \in \mathbb{R}^{3N_{bc}+N_F}\,. \end{aligned}$$

Next, define the convex hyper-cone $\mathcal{C}_f \equiv \mathcal{K}_{bc,1} \oplus \ldots \oplus \mathcal{K}_{bc,N_{bc}} \oplus \mathcal{B}_1 \oplus \ldots \oplus \mathcal{B}_{N_F}$ and its polar counterpart $\mathcal{C}_f^\circ \equiv \mathcal{K}_{bc,1}^\circ \oplus \ldots \oplus \mathcal{K}_{bc,N_{bc}}^\circ \oplus \mathcal{B}_1^\circ \oplus \ldots \oplus \mathcal{B}_{N_F}^\circ$. Here, $\mathcal{K}_{bc,i} \equiv \{[x,\ y,\ z]^T \in \mathbb{R}^3 :\quad 0 \le x \text{ and } \mu_i^{bc} x - \sqrt{y^2+z^2} \ge 0\}$ and $\mathcal{K}_{bc,i}^\circ$ is the associated polar cone. Defining $\mathbf{N}_f \equiv \mathbf{P}_f^T \mathbf{P}_f$, after algebraic manipulations [2], the discretized problem leads to a CCP: find $\boldsymbol{\nu}_f^{(l+1)}$ such that

$$\mathcal{C}_{f,k} \ni \boldsymbol{\nu}_{f,k}^{(l+1)} \quad \perp \quad -(\mathbf{p}_f + \mathbf{N}_f \boldsymbol{\nu}_f^{(l+1)})_k \in \mathcal{C}_{f,k}^\circ\,.$$

As shown in [2], this CCP represents the first order optimality condition [7] for the convex quadratic optimization problem with conic constraints

$$\begin{aligned} \boldsymbol{\nu}_f^{(l+1)} &= \min_{\boldsymbol{\nu}} \frac{1}{2} \boldsymbol{\nu}^T \mathbf{N}_f \boldsymbol{\nu} + \mathbf{p}_f^T \boldsymbol{\nu} \\ &\quad \text{subject to } \boldsymbol{\nu}_{f,k} \in \mathcal{C}_{f,k}\,. \end{aligned} \tag{17}$$

At $t^{(l+1)}$, the optimization problem is solved for $\boldsymbol{\nu}_f^{(l+1)}$ employing the same techniques used for the problem in Eq. (17). Upon finding $\boldsymbol{\nu}_f^{(l+1)}$, one has the set of Lagrange multipliers associated with enforcing the incompressibility constraints

$\lambda^{f,(l+1)}$, the non-penetration constraints $\gamma_{k,n}^{bc,(l+1)}$, and the mutual interaction at the fluid-wall interface $\gamma_{k,u}^{bc,(l+1)}$ and $\gamma_{k,w}^{bc,(l+1)}$. The new velocities $\mathbf{v}^{f,(l+1)}$ are computed expeditiously using Eq. (16b). Subsequently, the new SPH positions are computed using Eq. (16a).

4. The fluid–solid coupled dynamics problem

The coupled fluid–solid (FS) interaction solution builds on notation introduced in §2 and §3 as the discretized equations of motion are a straight splicing of the equations for the solid and fluid phases. A coupling force term comes into play by means of a projection operator $\mathbf{D}^{FS}$ that yields the generalized forces acting on a subset of SPH particles and the moving solid bodies that these particles interact with. The collection of all FS events at time $t^{(l)}$ provides the active set $\mathcal{A}^{(l),FS}(\mathbf{x}, \mathbf{q}, \delta_{FS})$. For an event $j \in \mathcal{A}^{(l),FS}$, the projection operator is defined as

$$\mathbf{D}_j^{FS} \equiv \left[\mathbf{0}_{3\times3}, \ldots, -\mathbf{A}_j^{FS,T}, \mathbf{0}_{3\times3}, \ldots, \mathbf{0}_{3\times3}, \ldots, \mathbf{A}_j^{FS,T}, \left(-\mathbf{A}_j^{FS,T}\mathbf{A}_B\tilde{\bar{\mathbf{s}}}_{j,B}\right)^T, \mathbf{0}_{3\times3}, \ldots\right]^T \in \mathbb{R}^{(3N_F+6n_b)\times 3},$$

where for unilateral event j, by convention, the first column is associated with the normal $\mathbf{n}_j^{FS}$ component of the force, while the other two columns of $\mathbf{D}_j^{FS}$ are tied to the $\mathbf{u}_j^{FS}$ and $\mathbf{w}_j^{FS}$ components of the tangential force. Above, $\mathbf{A}_j^{FS} \equiv [\mathbf{n}_j^{FS}, \mathbf{u}_j^{FS}, \mathbf{w}_j^{FS}] \in \mathbb{R}^{3\times3}$ is the orientation matrix associated with FS event j; $\mathbf{A}_B = \mathbf{A}(\boldsymbol{\epsilon}_B)$ is the rotation matrix of body B involved in event j; and, $\bar{\mathbf{s}}_{j,B}$ is the contact location in body B relative coordinates. Associated with event j is a Lagrange multiplier $\gamma_j^{FS} \in \mathbb{R}^3$ that yields the coupling force $\mathbf{D}_j^{FS}\gamma_j^{FS}$. The force impressed upon an SPH particle as a result of the non-penetration condition is registered with a flipped sign by the solid, which also experiences a corresponding torque. Insofar the FS projection operator is concerned, it can be represented in two equivalent forms:

$$\mathbf{D}_j^{FS} = \left[\mathbf{D}_{j,n}^{FS},\ \mathbf{D}_{j,u}^{FS},\ \mathbf{D}_{j,w}^{FS}\right] \equiv \begin{bmatrix} \mathbf{D}_j^F \\ \mathbf{D}_j^S \end{bmatrix} \in \mathbb{R}^{(3N_F+6n_b)\times 3},$$

with $\mathbf{D}^{FS} \equiv \left[\mathbf{D}_1^{FS}\ \mathbf{D}_2^{FS}\ \ldots\right] \in \mathbb{R}^{(3N_F+6n_b)\times 3N_{FS}}$, where $N_{FS} = |\mathcal{A}^{FS,(l)}|$. The discretized equations of motion for a coupled FS problem assume then the form

$$\begin{aligned}
\mathbf{x}^{(l+1)} &= \mathbf{x}^{(l)} + \Delta t\, \mathbf{v}^{f,(l+1)} \\
\mathbf{q}^{(l+1)} &= \mathbf{q}^{(l)} + \Delta t\, \mathbf{L}^s(\mathbf{q}^{(l)})\, \mathbf{v}^{(l+1)} \\
\mathbf{v}^{f,(l+1)} - \mathbf{v}^{f,(l)} &= \Delta t\, \mathbf{f}^f(t^{(l)}, \mathbf{x}^{(l)}, \mathbf{v}^{f,(l)}) + \mathbf{G}^f\lambda^{f,(l+1)} + \mathbf{D}^{bc}\gamma^{bc,(l+1)} + \mathbf{D}^F\gamma^{FS,(l+1)} \\
\mathbf{M}^s(\mathbf{v}^{(l+1)} - \mathbf{v}^{(l)}) &= \Delta t\, \mathbf{f}^s(t^{(l)}, \mathbf{q}^{(l)}, \mathbf{v}^{(l)}) + \mathbf{G}^s\lambda^{s,(l+1)} + \mathbf{D}^s\gamma^{s,(l+1)} + \mathbf{D}^S\gamma^{FS,(l+1)} \\
0 &= \frac{1}{\Delta t}\mathbf{g}^f(\mathbf{x}^{(l)}) + \mathbf{G}^{f,T}\mathbf{v}^{f,(l+1)} \\
0 &= \frac{1}{\Delta t}\mathbf{g}^s(\mathbf{q}^{(l)}, t^{(l)}) + \mathbf{G}^{s,T}\mathbf{v}^{(l+1)} + \mathbf{g}_t^s(\mathbf{q}^{(l)}, t^{(l)}) \\
k \in \mathcal{A}^{bc,(l)}\ &: \begin{cases} 0 \le \frac{C_k^{bc}(\mathbf{x}^{(l)})}{\Delta t} + \mathbf{D}_{k,n}^{bc,T}\mathbf{v}^{f,(l+1)} - \mu_k^{bc}\sqrt{\left(\mathbf{D}_{k,u}^{bc,T}\mathbf{v}^{f,(l+1)}\right)^2 + \left(\mathbf{D}_{k,w}^{bc,T}\mathbf{v}^{f,(l+1)}\right)^2} \perp \gamma_{k,n}^{bc,(l+1)} \ge 0 \\ \left(\gamma_{k,u}^{bc,(l+1)}, \gamma_{k,w}^{bc,(l+1)}\right) = \underset{\sqrt{\gamma_u^2+\gamma_w^2} \le \mu_k^{bc}\gamma_{k,n}^{bc,(l+1)}}{\operatorname{argmin}} \mathbf{v}^{f,(l+1),T}\left(\gamma_u\mathbf{D}_{k,u}^{bc} + \gamma_{k,w}\mathbf{D}_{k,w}^{bc}\right) \end{cases} \\
i \in \mathcal{A}^{s,(l)}\ &: \begin{cases} 0 \le \frac{C_i^s(\mathbf{q}^{(l)})}{\Delta t} + \mathbf{D}_{i,n}^{s,T}\mathbf{v}^{(l+1)} - \mu_i^s\sqrt{(\mathbf{D}_{i,u}^{s,T}\cdot\mathbf{v}^{(l+1)})^2 + (\mathbf{D}_{i,w}^{s,T}\cdot\mathbf{v}^{(l+1)})^2} \perp \gamma_{i,n}^{s,(l+1)} \ge 0 \\ \left(\gamma_{i,u}^{s,(l+1)}, \gamma_{i,w}^{s,(l+1)}\right) = \underset{\sqrt{\gamma_u^2+\gamma_w^2} \le \mu_i^s\gamma_{i,n}^{s,(l+1)}}{\operatorname{argmin}} \mathbf{v}^T\cdot\left(\gamma_u\,\mathbf{D}_{i,u}^s + \gamma_w\,\mathbf{D}_{i,w}^s\right). \end{cases} \\
j \in \mathcal{A}^{FS,(l)}\ &: \begin{cases} 0 \le \frac{C_j^{FS}(\mathbf{x}^{(l)},\mathbf{q}^{(l)})}{\Delta t} + \mathbf{D}_{j,n}^{FS,T}\mathbf{z}^{(l+1)} - \mu_j^{FS}\sqrt{\left(\mathbf{D}_{j,u}^{FS,T}\mathbf{z}^{(l+1)}\right)^2 + \left(\mathbf{D}_{j,w}^{FS,T}\mathbf{z}^{(l+1)}\right)^2} \perp \gamma_{j,n}^{FS,(l+1)} \ge 0 \\ \left(\gamma_{j,u}^{FS,(l+1)}, \gamma_{j,w}^{FS,(l+1)}\right) = \underset{\sqrt{\gamma_u^2+\gamma_w^2} \le \mu_j^{FS}\gamma_{j,n}^{FS,(l+1)}}{\operatorname{argmin}} \mathbf{z}^{(l+1),T}\left(\gamma_u\mathbf{D}_{j,u}^{FS} + \gamma_w\mathbf{D}_{j,w}^{FS}\right) \end{cases}
\end{aligned}$$

where $\mathbf{z} = \left[\mathbf{v}^{f,T}, \mathbf{v}^{s,T}\right]^T \in \mathbb{R}^{3N_F+6n_b}$ are the system-level generalized velocities. This coupled problem is reformulated as

$$\mathbf{y}^{(l+1)} = \mathbf{y}^{(l)} + \Delta t\, \mathbf{L}^{(l)}\mathbf{z}^{(l+1)} \tag{19a}$$

$$\mathbf{M}(\mathbf{z}^{(l+1)} - \mathbf{z}^{(l)}) = \Delta t\, \mathbf{f}(t^{(l)}, \mathbf{y}^{(l)}, \mathbf{z}^{(l)}) + \mathbf{G}\lambda^{(l+1)} + \mathbf{D}\gamma^{(l+1)} \tag{19b}$$

$$0 = \mathbf{g} + \mathbf{G}^T\mathbf{z}^{(l+1)} \tag{19c}$$

$$j \in \mathcal{A}^{(l)} \ : \ \begin{cases} 0 \le \frac{C_j(\mathbf{y}^{(l)})}{\Delta t} + \mathbf{D}_{j,n}^T\mathbf{z}^{(l+1)} - \mu_j\sqrt{\left(\mathbf{D}_{j,u}^T\mathbf{z}^{(l+1)}\right)^2 + \left(\mathbf{D}_{j,w}^T\mathbf{z}^{(l+1)}\right)^2} \perp \gamma_{j,n}^{(l+1)} \ge 0 \\ \left(\gamma_{j,u}^{(l+1)}, \gamma_{j,w}^{(l+1)}\right) = \underset{\sqrt{\gamma_u^2+\gamma_w^2} \le \mu_j \gamma_{j,n}^{(l+1)}}{\operatorname{argmin}} \quad \mathbf{z}^{(l+1),T}\left(\gamma_u \mathbf{D}_{j,u} + \gamma_w \mathbf{D}_{j,w}\right) . \end{cases} \tag{19d}$$

When advancing the system state from $t^{(l)}$ to $t^{(l+1)}$, the system-level active set associated with the unilateral events $\mathcal{A}^{(l)} \equiv \mathcal{A}^{s,(l)} \cup \mathcal{A}^{bc,(l)} \cup \mathcal{A}^{FS,(l)}$ is identified using a collision detection/proximity computation analysis carried out at $t^{(l)}$. In a broad sense, the term "unilateral event" for j in Eq. (19d) is used in conjunction with a contact event between two solids, a boundary condition interaction between an SPH particle and a wall, or a two-way coupling condition between an SPH particle and a moving solid. Two sets of Lagrange multipliers λ and γ are associated with equality kinematic constraints and unilateral events, respectively. For the former, $\lambda^f \in \mathbb{R}^{N_F}$ and $\lambda^s \in \mathbb{R}^{N_B}$; for the latter, $\gamma^s \in \mathbb{R}^{3N_K}$, $\gamma^{bc} \in \mathbb{R}^{3N_{bc}}$, and $\gamma^{FS} \in \mathbb{R}^{3N_{FS}}$, respectively. In the end,

$$\gamma \equiv \begin{bmatrix} \gamma^{bc} \\ \gamma^s \\ \gamma^{FS} \end{bmatrix} \in \mathbb{R}^{3(N_{bc}+N_K+N_{FS})} , \quad \lambda \equiv \begin{bmatrix} \lambda^f \\ \lambda^s \end{bmatrix} \in \mathbb{R}^{N_F+N_B} .$$

Three vector quantities used in Eq. (19): the generalized positions, generalized forces, and equality constraint violations, respectively, are defined as

$$\mathbf{y} \equiv \begin{bmatrix} \mathbf{x} \\ \mathbf{q} \end{bmatrix} \in \mathbb{R}^{3N_F+7n_b} , \quad \mathbf{f} \equiv \begin{bmatrix} \mathbf{f}^f \\ \mathbf{f}^s \end{bmatrix} \in \mathbb{R}^{3N_F+6n_b} , \quad \mathbf{g} \equiv \begin{bmatrix} \frac{1}{\Delta t}\mathbf{g}^f(\mathbf{x}^{(l)}) \\ \frac{1}{\Delta t}\mathbf{g}^s(\mathbf{q}^{(l)}, t^{(l)}) + \mathbf{g}_t^s \end{bmatrix} \in \mathbb{R}^{N_F+N_B} . \tag{20}$$

Several matrix quantities are defines as follows. First, the coefficient matrix in the complementarity conditions is called $\mathbf{D}$; the coefficient matrix in the velocity-level kinematic constraints is $\mathbf{G}$:

$$\mathbf{D} \equiv \begin{bmatrix} \mathbf{D}^{bc} & \mathbf{0} & \mathbf{D}^F \\ \mathbf{0} & \mathbf{D}^s & \mathbf{D}^S \end{bmatrix} \in \mathbb{R}^{(3N_F+6n_b)\times 3(N_{bc}+N_K+N_{FS})} , \quad \mathbf{G} \equiv \begin{bmatrix} \mathbf{G}^f & \mathbf{0} \\ \mathbf{0} & \mathbf{G}^s \end{bmatrix} \in \mathbb{R}^{(3N_F+6n_b)\times(N_F+N_B)} .$$

Second, the system-level mass matrix and the transformation matrix that ties the generalized velocities to the first time derivative of the generalized positions are defined as

$$\mathbf{M} \equiv \begin{bmatrix} \mathbf{I}_{3N_F} & \mathbf{0}_{3N_F\times 6n_b} \\ \mathbf{0}_{6n_b\times 3N_F} & \mathbf{M}^s \end{bmatrix} , \quad \mathbf{L} \equiv \begin{bmatrix} \mathbf{I}_{3N_F} & \mathbf{0}_{3N_F\times 6n_b} \\ \mathbf{0}_{7n_b\times 3N_F} & \mathbf{L}^s \end{bmatrix} .$$

Let

$$\mathbf{d}_i \equiv [\frac{1}{\Delta t}C_i^{(l)},\ 0,\ 0]^T + \mathbf{D}_i^{(l),T}(\mathbf{z}^{(l)} + \Delta t\, \mathbf{M}^{-1}\mathbf{f}) \in \mathbb{R}^3$$
$$b_j \equiv \mathbf{g}_j^{(l)} + \mathbf{G}_j^{(l),T}(\mathbf{z}^{(l)} + \Delta t\, \mathbf{M}^{-1}\mathbf{f}) \in \mathbb{R} ,$$

and define

$$\begin{aligned} \mathbf{P} &\equiv \begin{bmatrix} \mathbf{D} & \mathbf{G} \end{bmatrix} \in \mathbb{R}^{(3N_F+6n_b)\times[3(N_{bc}+N_K+N_{FS})+N_F+N_B]} , \\ \boldsymbol{\nu}^{(l+1)} &\equiv \begin{bmatrix} \gamma^{(l+1)} \\ \lambda^{(l+1)} \end{bmatrix} \\ \mathbf{p}_f &\equiv \left[\mathbf{d}_1^{f,T}, \dots, \mathbf{d}_{N_K}^{f,T}, b_1^f, \dots, b_{N_B}^f\right]^T \in \mathbb{R}^{3(N_{bc}+N_K+N_{FS})+N_F+N_B} . \end{aligned} \tag{21}$$

Next, define $\mathbf{N} \equiv \mathbf{P}^T\mathbf{M}^{-1}\mathbf{P}$, the convex hyper-cone $\mathcal{C}_{FS} \equiv \mathcal{K}_{FS,1} \oplus \dots \oplus \mathcal{K}_{FS,N_{FS}}$, and its polar counterpart $\mathcal{C}_{FS}^\circ \equiv \mathcal{K}_{FS,1}^\circ \oplus \dots \oplus \mathcal{K}_{FS,N_{FS}}^\circ$. Here, $\mathcal{K}_{FS,i} \equiv \{[x,\ y,\ z]^T \in \mathbb{R}^3 : \quad 0 \le x \text{ and } \mu_i^{FS}x - \sqrt{y^2+z^2} \ge 0\}$ and $\mathcal{K}_{FS,i}^\circ$ is the associated polar cone. After algebraic manipulations [2], the discretized problem leads to a CCP: find $\boldsymbol{\nu}^{(l+1)}$ such that

$$\mathcal{C}_k \ni \boldsymbol{\nu}_k^{(l+1)} \quad \perp \quad -(\mathbf{p} + \mathbf{N}\boldsymbol{\nu}^{(l+1)})_k \in \mathcal{C}_k^\circ , \tag{22}$$

where $\mathcal{C} \equiv \mathcal{C}_s \oplus \mathcal{C}_f \oplus \mathcal{C}_{FS}$. Following the approach [2], this CCP can be shown to represent the first order optimality condition [7] for the convex quadratic optimization problem with conic constraints

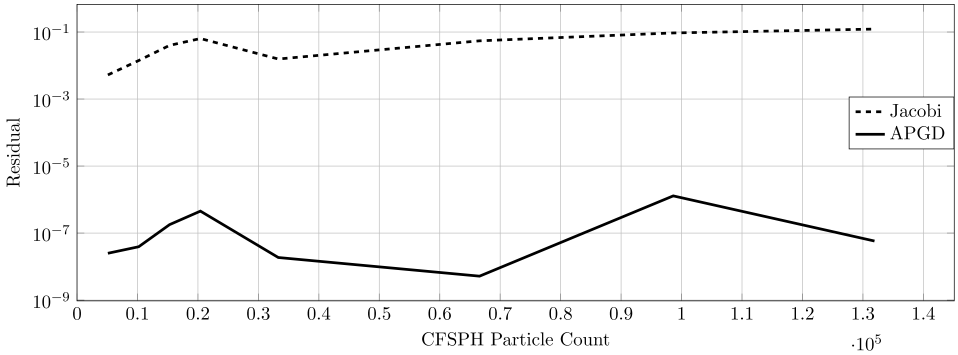

Fig. 3. Log of solver residual vs. CFSPH particle count. The iteration budget was 800 for both Jacobi and APGD.

$$\begin{aligned} \boldsymbol{\nu}^{(l+1)} &= \min_{\boldsymbol{\nu}} \frac{1}{2}\boldsymbol{\nu}^T \mathbf{N}\boldsymbol{\nu} + \mathbf{p}^T\boldsymbol{\nu} \\ & \text{subject to } \boldsymbol{\nu}_k^{(l+1)} \in \mathcal{C}_k \, . \end{aligned} \tag{23}$$

At each $t^{(l+1)}$, the optimization problem above is solved for $\boldsymbol{\nu}^{(l+1)}$ by using a Nesterov or Barzilai–Borwein type solution [41,42]. Upon finding the numerical solution of the optimization problem, one has the set of Lagrange multipliers that enforces the collection of unilateral and the bilateral constraints. A new system configuration at the velocity level $\mathbf{z}^{(l+1)}$ is computed via Eq. (19b). Along with a new set of velocities goes a set of generalized positions computed via Eq. (19a).

5. Numerical experiments

CFSPH has been implemented in an open source simulation engine called Chrono [43,44]. Therein, three parallel algorithms compute the active sets $\mathcal{A}^{s,(l)}$, $\mathcal{A}^{bc,(l)}$, and $\mathcal{A}^{FS,(l)}$. As the solid bodies vary in size vastly, a broad-phase step is performed to prune bodies that are not in contact in order to determine a list of *potential* contact pairs. This list is subsequently processed using a Minkowski Portal Refinement algorithm [45,46] to provide actual contact information. Proximity computation for the SPH particles relies on a customized spatial subdivision algorithm that leverages their equal-size compact support attribute [47]. The fluid-particle/solid-body proximity computation uses the grid involved in the broad-phase step for solid bodies. The implementation relies on parallel computing via OpenMP [48] and the Blaze library [49].

5.1. A CCP solver comparison for the CFSPH approach

The computational bottleneck in CFSPH is associated with the solution of the optimization problem in Eq. (23). For larger problems, see, for instance, §5.5, the optimization problem is posed in millions of variables and brings forward millions of conic and equality constraints. In this section we highlight the performance of the Accelerated Projected Gradient Descent (APGD) method, which is a Nesterov-type algorithm [50] recently introduced in [41] to handle large CCPs. We compare APGD's performance to that of Projected Jacobi, the go-to *parallel* solver for handling CCPs like the one in Eq. (22), to demonstrate that solvers such as APGD or Barzilai–Borwein [42], render the proposed solution methodology effective.

In a first numerical experiment the number of SPH particles in a rectangular container was gradually increased to assess convergence speed. Both Jacobi and APGD performed exactly 800 iterations towards solving the CCP at $t^{(l)} > t^{(0)}$ using $\Delta t = 1\text{e}{-}3$ s. Each SPH particle had a mass of 0.02 kg, a kernel radius of 0.032 m, and a rest density of 1000 kg/m^3. For all numerical experiments herein, all quantities are expressed in SI units unless explicitly stated otherwise. For various particle counts, Fig. 3 shows that in 800 iterations APGD achieves a residual r several orders of magnitude smaller in approximately the same amount of time as Jacobi (see also Fig. 4). Using notation introduced in Eqs. (22) and (23) and the cone projection operator $\Pi_{\mathcal{C}}$ [41], the residual r, which is a metric used in the CFSPH stopping criteria, is defined as

$$r \equiv \|\psi\|_2, \quad \text{where} \quad \psi \equiv \frac{1}{g_d}\left(\boldsymbol{\nu} - \Pi_{\mathcal{C}}\left(\boldsymbol{\nu} - g_d\left(\mathbf{N}\boldsymbol{\nu} + \mathbf{p}\right)\right)\right) \quad \text{and} \quad g_d \equiv \frac{1}{|\mathcal{A}^{(l)}|^2} \, .$$

Note that if $\boldsymbol{\nu} = \boldsymbol{\nu}^*$ is optimal, then $\Pi_{\mathcal{C}}\left(\boldsymbol{\nu}^* - g_d\left(\mathbf{N}\boldsymbol{\nu}^* + \mathbf{p}\right)\right) = \boldsymbol{\nu}^*$, so $\psi = \mathbf{0}$. Conversely, if $\boldsymbol{\nu}$ is not optimal, $\Pi_{\mathcal{C}}\left(\boldsymbol{\nu} - g_d\left(\mathbf{N}\boldsymbol{\nu} + \mathbf{p}\right)\right) = \boldsymbol{\nu} - g_d\psi$. The left hand side is equivalent to taking a steepest descent step of length g_d and projecting back onto the feasible set $\mathcal{C}$ via $\Pi_{\mathcal{C}}$. The right hand side says that the same point is reached by taking a step of length g_d in the direction opposite of ψ. A low value for ψ and thus for r suggests that the algorithm reached, or is close to, an equilibrium point.

Fig. 4 presents a scaling analysis – for various problem sizes it reports the amount of time required to perform the said 800 iterations. Jacobi and APGD scale linearly with problem size and require comparable amounts of time, yet the APGD solution is "more converged" (see Fig. 3). The results were obtained on a 40 core Intel Xeon® CPU E5-2650 v3 @ 2.30 GHz

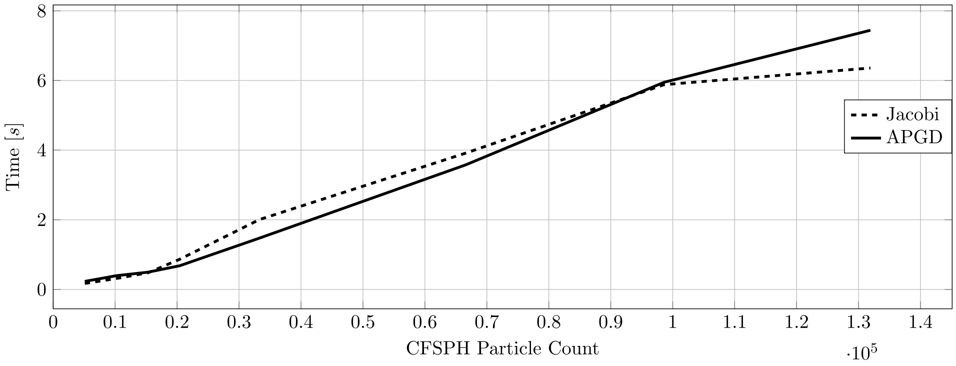

Fig. 4. Time taken to perform 800 iterations for different number of CFSPH particles.

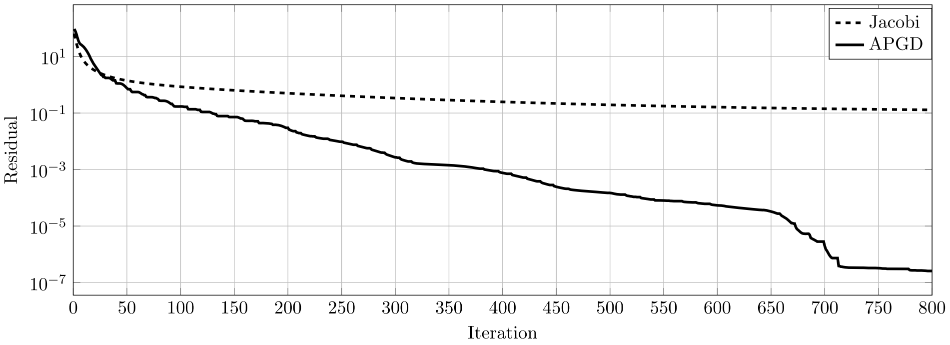

Fig. 5. Log residual vs. iteration count for a CFSPH simulation with 131 918 particles.

CPU using 128 GB of DDR4 2133 MHz memory. Finally, Fig. 5 illustrates the decrease of r during one time step when simulating 131 918 CFSPH particles.

5.2. Compressibility analysis

In this experiment we monitor the time evolution of the density for a fluid stored in a rectangular container of dimensions 1.1 m × 1.1 m × 1.2 m (length/width/height). There are $N_F = 57\,735$ inviscid fluid particles; each particle has a mass of 0.02 kg, a kernel radius of 0.032 m and a rest density of $\rho_0 = 1000$ kg/m^3. The particles are moving under the influence of internal forces and gravity. Fig. 6 reports levels of error in enforcing incompressibility. At time $t^{(l)}$, the vertical axis shows the relative error

$$\%\,\text{error}^{(l)} \equiv \left(\frac{1}{\rho_0 N_F}\sum_{i=1}^{N_F} \rho_i^{(l)} - 1\right) \times 100\,.$$

The solver tolerance, which is tied to the residual r of section §5.1, was gradually tightened: 1e−1, 1e−2, 1e−3, 1e−4, 1e−6, and 1e−8. The analysis was carried out for a 10 second time span and Fig. 6 shows error values for the last two seconds of simulation. As expected, smaller residuals r; i.e., more stringent stopping criteria, led to more accurate results.

Next, we report on an experiment to illustrate that the proposed numerical solution, relative to the weakly compressible solution, operates at large times, a consequence of the (i) unified approach used to handle the solid and fluid phases; and, (ii) the use of a half-implicit symplectic integration method borrowed from solid mechanics. To this end, we contrast CFSPH with the open-source solver DualSPHysics [51], which is anchored in an WCSPH-type approach outlined in §3.2.1. The CFSPH solution, found using the Barzilai–Borwein solver in Chrono[42], was used with $r = 10^{-8}$. For DualSPHysics, the CFL number is set to 0.1 and the speed of sound c_s, see Eq. (10), is chosen to obtain several levels of compressibility. Fig. 7 confirms that the level of compressibility in WCSPH is controlled via c_s. As shown with solid lines, increasing c_s leads to smaller density errors. However, higher c_s values translate into stiffer problems that require smaller integration step sizes. Thus, at one end of the spectrum, WCSPH uses small yet computationally inexpensive time steps. At the other end of the spectrum, CFSPH uses a half-implicit numerical integrator that allows for large albeit computationally heavy times steps. Against this backdrop, Fig. 7 answers the following question: what value of c_s and Δt_{CFSPH} should be used for DualSPHysics and CFSPH, respectively, so that the quality of the solutions produced by these two solvers is comparable? Note that by choosing a tolerance of 1e−8 for the CCP, both the CFSPH solution quality as well as the simulation duration

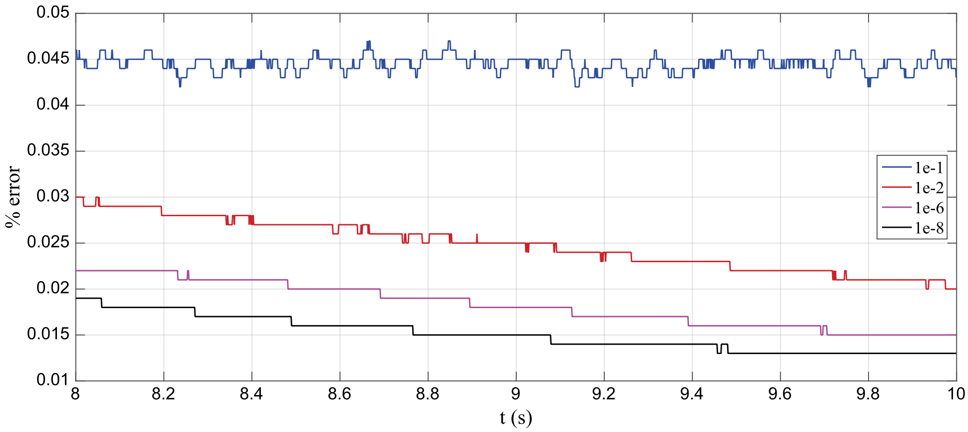

Fig. 6. CFSPH: sensitivity of compressibility relative error with respect to solver tolerance.

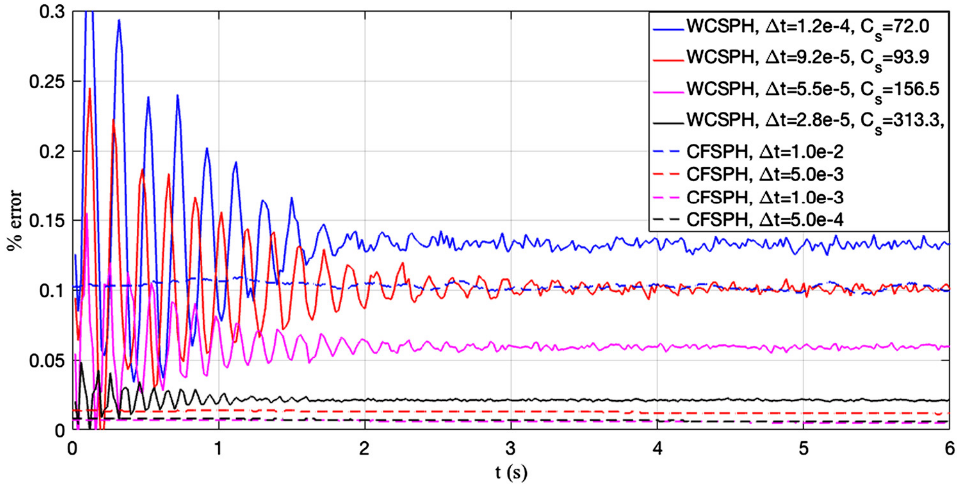

Fig. 7. CFSPH vs. WCSPH (DualSPHysics [51]) comparison for relative error in compressibility level. Only first six seconds out of 20 second long simulation shown.

are exclusively controlled by the size of Δt. Indeed, CFSPH and DualSPHysics solutions that are qualitatively the same are obtained when using $\Delta t_{CFSPH} = 1\mathrm{e}{-2}$ and respectively $c_s = 93.9$ m/s, which leads to $\Delta t_{WCSPH} = 9.2\mathrm{e}{-5}$. This indicates that DualSPHysics will take approximately 100× more integration steps to accomplish the same level of accuracy, albeit each step will be significantly faster than one CFSPH time step. Against backdrop, when the two solvers produced a similar quality solution, they required about the same amount of time to finish the 20 s long simulation. Overall, CFSPH was 1.5× faster than WCSPH when $\Delta t_{WCSPH} = 9.2\mathrm{e}{-5}$ and $\Delta t_{CFSPH} = 1\mathrm{e}{-2}$. It should be pointed out that no systematic attempt was made to tune either solver and a comparison in terms of efficiency fell outside the scope of this contribution. The simulations were performed on a 40 core Intel(R) Xeon® CPU E5-2650 v3 @ 2.30 GHz processor with 128 GB of DDR4 2133 MHz memory.

5.3. Dam break analysis

The collapse of a liquid column is a standard test performed to validate an SPH implementation. To that end, we simulate the water-front propagation of a $L = 1$ cube of water placed on the leftmost side of a cubic container and released over a dry bed at $t(gH)^{1/2} = 0$. In the 3D case studied the flow is inviscid and $g = 1$. In Fig. 8, we compare the non-dimensional front position x_{front}/H as a function of the time scale, $t(gH)^{1/2}$, against experimental [52] and simulation results [21]. At early stages, CFSPH agrees well with the experiment, yet it gradually over-predicts the experimental results after $t(gH)^{1/2} \approx 2$. We attribute this discrepancy to the inviscid flow assumption which becomes inaccurate as the flow speed ($\propto$ tangent line in Fig. 8) increases and the effect of the viscosity term, $\nabla^2 \mathbf{v}$, in the Navier–Stokes equations becomes significant. Moreover, smaller front propagation speeds are expected for viscous fluids. Thus, it stands to a reason that the numerical results over-estimate the experimental results.

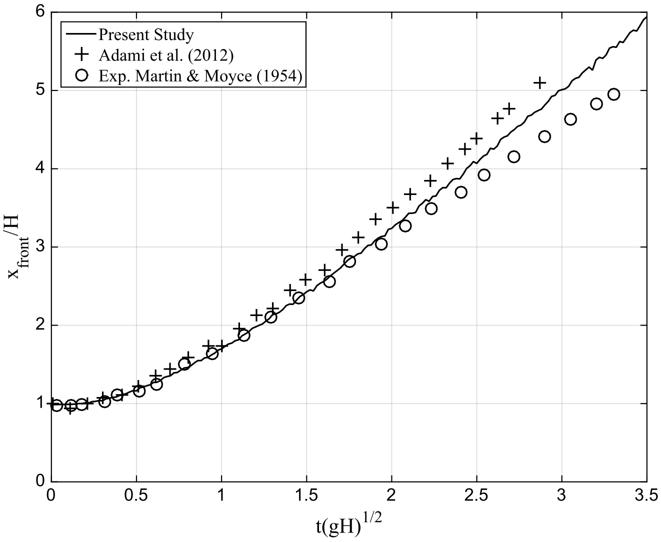

Fig. 8. Water-front propagation study of dam break analysis.

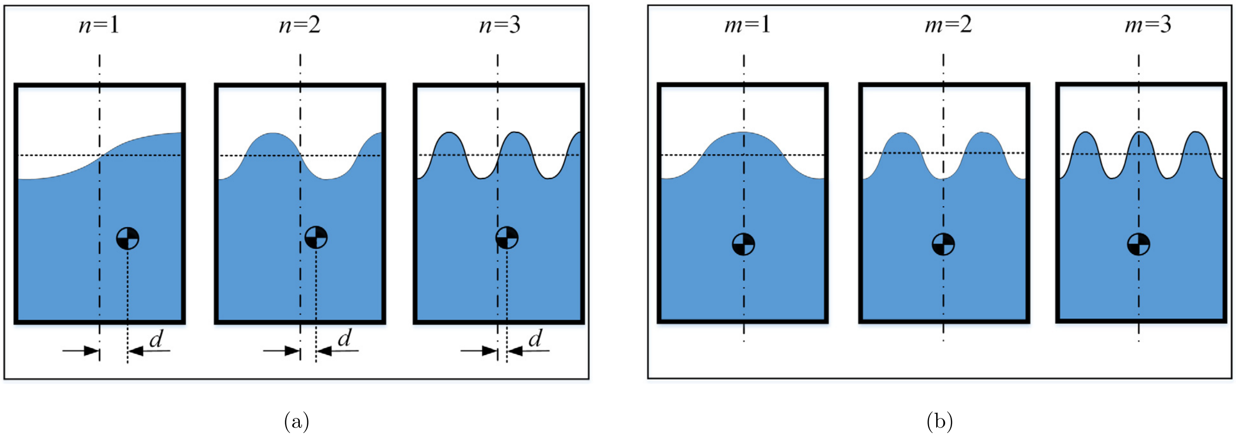

(a) (b)

Fig. 9. Wave shape in sloshing [53]: (a) asymmetric waves; (b) symmetric waves. Mode numbers m and n associated with symmetric and asymmetric modes, respectively; d is the horizontal displacement of the center of mass from the stationary location in the left-to-right, in-plane direction. Gravitational acceleration is vertical, pointing down.

5.4. Sloshing simulation

Under an inviscid flow assumption, there are 2D fluid sloshing scenarios that can be characterized analytically. Consider a rectangular tank filled with fluid to a height h and subject to a forced vibration of the form $X_0\, sin(ft)$, see Fig. 9. According to [53], the analytical solution for the free surface profile is a combination of series of symmetric and asymmetric motion modes. The natural frequencies of the antisymmetric, ω_n, and symmetric modes, ω_m, can be expressed as

$$\omega_n^2 = (2n-1)\,\pi\left(\frac{g}{w}\right)\tanh\left[(2n-1)\,\pi\left(\frac{h}{w}\right)\right]$$
$$\omega_m^2 = 2m\pi\left(\frac{g}{w}\right)\tanh\left[2m\pi\left(\frac{h}{w}\right)\right],$$

where n and m are mode numbers, g is the value of the gravitational acceleration, and w is the tank width; i.e., the tank dimension in the direction of oscillation. The relations above imply that the natural frequencies of the symmetric modes are all higher than the corresponding antisymmetric frequencies. Since there is no lateral motion of the fluid center of mass for symmetric modes, they produce no net lateral force/torque on the sloshing tank.

The eigenfunctions slosh modes are the basis for evaluating the solution of a forced vibration. Consequently, the net force exerted on a sloshing tank in a forced vibration can be expressed as [53]

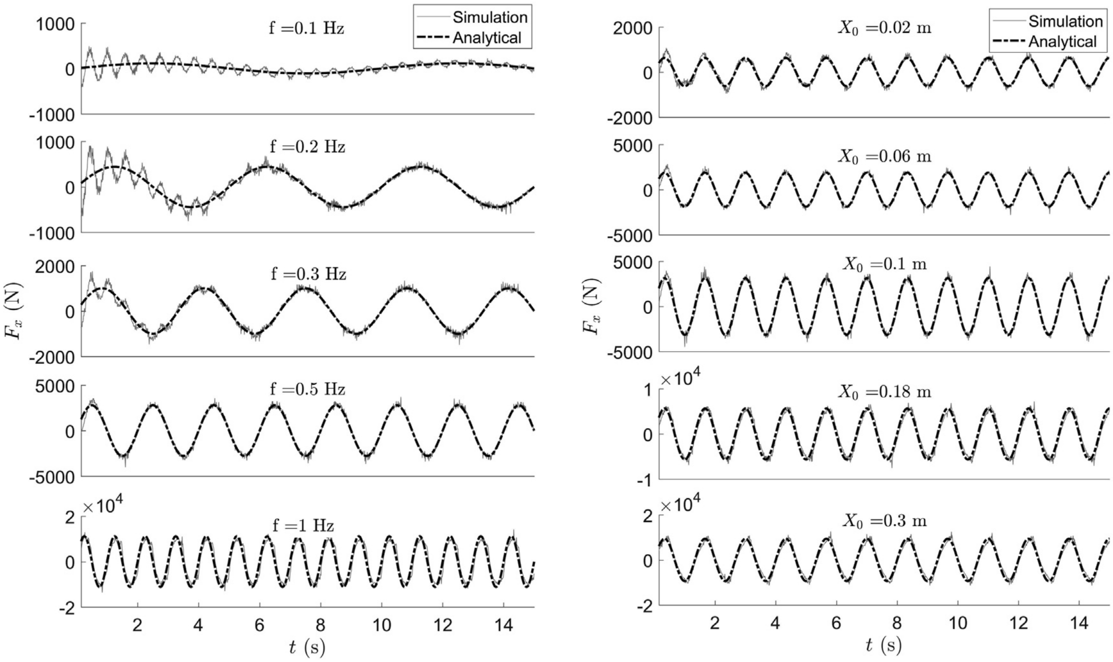

(a) (b)

Fig. 10. Net force on the sloshing tank. The tank was subjected to a lateral X_0 $sin(2\pi ft)$ forced vibration. Sub-figures (a) and (b) list the force magnitude for different vibration frequency (f) and amplitude (X_0), respectively.

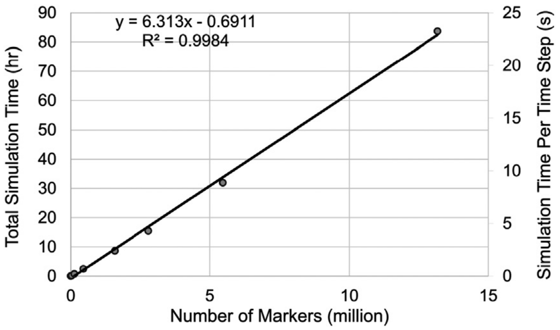

Fig. 11. Scaling analysis for sloshing problem shows linear increase in compute time with respect to the number of SPH particles involved in the simulation.

$$\frac{F_{x_0}}{f^2 X_0 m_l} = 1 + 8\frac{w}{h}\sum_{n=1}^{N}\frac{\tanh\left[(2n-1)\pi h/w\right]}{(2n-1)^3\pi^3}\frac{f^2}{\omega_n^2 - f^2},$$

where F_{x_0} is the amplitude of the oscillation force, f and X_0 are the frequency and magnitude of the forced vibration, and m_l is the mass of the liquid. A comparison of the analytical and simulation results is provided in Fig. 10, where the force on the sloshing tank in the vibration direction is plotted for several f and X_0 values. For all tests, the tank and fluid were initially at rest and a sinusoidal motion was applied thereafter. Except for the transient regime, for which the analytical solution is not valid, the CFSPH results are in good agreement with the analytical solution. Some discrepancies are noted at low frequency, which we attribute to the transient behavior since the simulation considers a scenario where the tank starts its motion from rest. Moreover, the analytical solution focuses only on the steady-state solution. The small high-frequency, small-amplitude vibration in the force magnitude obtained from the simulation can be decreased arbitrarily by choosing tighter convergence criteria. Please note that there is no physical damping, such as viscosity, to damp the small oscillations.

We close the sloshing test with a scaling analysis to underline an attractive attribute of the proposed solution: linear scaling with problems size. Fig. 11 reports results for the sloshing test, from 2101 up to 13 180 420 SPH particles. The state variables that we carry with each particle are three positions, three velocities, a density and a pressure, which leads for the largest test to a problem with approximately 105 million states.

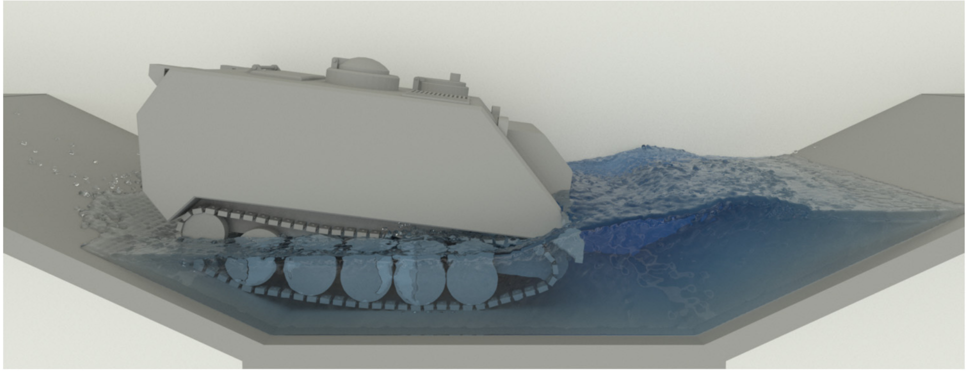

Fig. 12. Notional Tracked Vehicle performing fording operation. At each time step, an optimization problem in more than two million variables is solved, see Eq. (23).

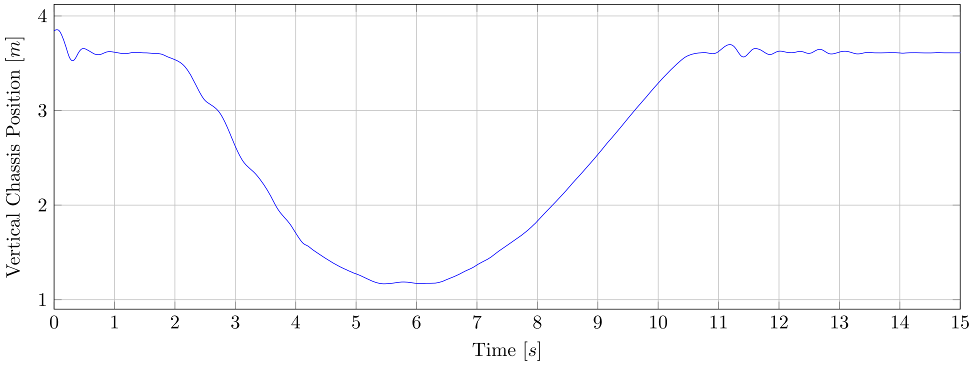

Fig. 13. Vertical position of a notional tracked vehicle chassis as it traverses the fording setup.

5.5. Fording analysis

In this section we scrutinize the fluid–solid coupling abilities of CFSPH by bringing into play a large number of rigid bodies and bilateral kinematic constraints associated with mechanical joints: e.g., revolute joints, spherical joints, etc. The problem investigated is that of a tracked vehicle fording, see Fig. 12. The vehicle has been modeled using Chrono::Vehicle [54] and contains two sets of tracks, each with 63 track shoes, a driven sprocket, an idler and five rollers. Each track shoe has a mass of 8.02 kg; each roller has a mass of 561.1 kg; the suspension arm mass is 75.26 kg; the sprocket's mass is 436.7 kg; the idler has a mass of 479.5 kg. In total, each set of tracks has a mass of 5233.26 kg. With a chassis mass of 5489.24 kg, the total vehicle mass is 15 973.8 kg. The idler is connected to the chassis via a carrier apparatus modeled as a translational spring damper-actuator to yield a hydraulic tensioner used for track preload. The chassis is connected to each set of tracks through five independent suspensions acting between each roller wheel and the chassis. The vehicle's engine drives the two sprockets, one on each track, independently allowing it to perform turning maneuvers. The model has $n_b = 154$ rigid bodies connected together through $N_B = 761$ bilateral kinematic constraints with collisions being modeled using a total of 544 different convex shapes. For collision detection purposes, the chassis is represented as a collection of convex hulls closely approximating the original non-convex chassis geometry so that contact with the fluid is captured accurately. Each track shoe, the idler and the rollers are made up of convex primitives such as cylinders and boxes. For further details about the model see [55,56].

The vehicle uses a driver model that locks the steering and attempts to maintain a constant speed of 2 m/s using a PID controller for throttle and braking. The fording setup consists of two end platforms approximately 6.096 m (20 ft) long followed by a slope of length 5.18 m (17 ft) and a bottom slope of length 4.57 m (15 ft). The distance from the end platform to the bottom was 2.43 m (8 ft) and was filled with fluid such that half of the vehicle would be under water during the fording operation. Each of the 1 426 663 SPH particles had a mass of 3.96e−3 kg, a kernel radius of 0.032 m and a rest density of 1000 kg/m^3. The simulation was 20 s long; the integration step size was $\Delta t = 0.001$ s; the CCP solver used was Barzilai–Borwein [42]. Fig. 13 shows the vertical position of the chassis center of mass as a function of time. Results for the vehicle velocity, throttle/breaking and engine torque are shown in Fig. 14. Note that while the throttle/brake controller is trying to enforce a 2 m/s velocity, the vehicle is often not traveling at exactly 2 m/s as it slides down the incline, moves through the water and then climbs up the incline. The simulation, which required 59 hours of run time, was executed on

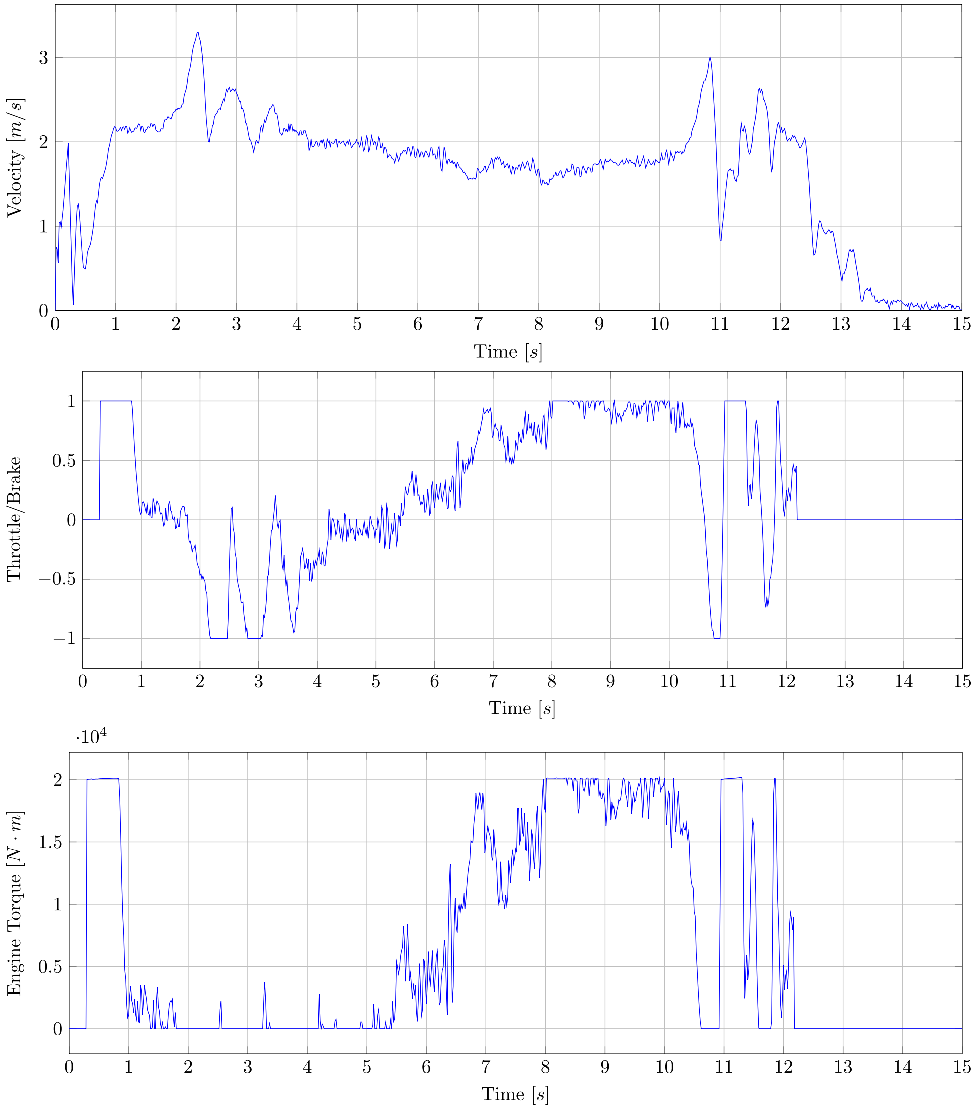

Fig. 14. Performing a fording operation using a notional tracked vehicle. (Top) Magnitude of chassis velocity over time; (Middle) Throttle/braking input for vehicle; (Bottom) Engine torque during driving operation.

a 40 core Intel(R) Xeon® CPU E5-2650 v3 @ 2.30 GHz processor with 128 GB of DDR4 2133 MHz memory. A simulation animation is available at [57], movie #129.

6. Conclusions and future work

We employ a differential variational approach used in rigid body dynamics to handle the dynamics of the fluid phase, which is spatially discretized via SPH. The boundary conditions as well as the fluid–solid coupling are captured via complementarity and maximum dissipation conditions enforced at the fluid–solid interface. The time–domain problem is posed as a large coupled system of differential, equality, and complementarity equations, which act as constraints on a set of optimization problems, the latter associated with the maximum dissipation conditions induced by the presence of internal friction. Upon time discretization via a half-implicit symplectic Euler method, a nonlinear complementarity problem is relaxed to a CCP which is solved using customized Nesterov or Barzilai–Borwein methods. The approach has been implemented into an open source simulation infrastructure and shown to scale linearly. The software implementation, which runs in parallel on one node using the OpenMP standard, has been validated using a compressibility test, a classical dam breaking scenario, and a sloshing test for which an analytical solution is available. A fording simulation of a tracked vehicle has been used to challenge the approach via a large coupled problem with tens of rigid bodies, millions of bilateral kinematics constraints, and more than a million SPH particles.

Unlike a previous effort that enforced incompressibility via a kinematic constraint [36], we maintained the nonlinear nature of the dissipation problem by not reverting to a linearization of the friction cones. This and/or the more effective CCP solvers employed might explain a significant improvement in enforcing the fluid incompressibility. Compared to the approach in [35], the methodology proposed goes beyond exclusive treatment of the fluid phase by bringing into discussion the coupling to moving solids into one unitary modeling framework that draws on differential variational inequalities.

Many aspects of the proposed solution could be improved upon and/or need further investigation. All simulations have been run under the assumption of an inviscid fluid. Moreover, the current scheme assumes an explicit-in-time treatment of the viscous force, something that could be revisited. It remains to be seen to what extent the maximum dissipation principle borrowed from handling friction and contact in solid dynamics is a suitable mechanism for handling boundary layer effects. In other words, it remains to investigate to what extent SPH endowed with a maximum dissipation principle is a good proxy for the physics controlling boundary layer phenomena. To speed up the simulation, certain solution components, e.g. proximity computation and SPH force evaluation, would benefit from execution on the GPU. Finally, handling surface tension via a kinematic constraint-based approach would enable the modeling of more complex physics in one unitary solution framework.

Acknowledgements

This research was supported in part by US Army TARDEC Rapid Innovation Fund grant W56HZV-14-C-0254. The research was made possible in part by the National Science Foundation grant CMMI 1635004.

Disclaimer: Reference herein to any specific commercial company, product, process, or service by trade name, trademark, manufacturer, or otherwise, does not necessarily constitute or imply its endorsement, recommendation, or favoring by the United States Government or the Department of the Army (DoA). The opinions of the authors expressed herein do not necessarily state or reflect those of the United States Government or the DoA, and shall not be used for advertising or product endorsement purposes.

References

[1] H. Mazhar, Physics Based Simulation Using Complementarity and Hybrid Lagrangian–Eulerian Methods, PhD thesis, University of Wisconsin, Madison, 2016.
[2] D. Negrut, R. Serban, A. Tasora, Posing multibody dynamics with friction and contact as a differential complementarity problem, J. Comput. Nonlinear Dyn. 13 (1) (2017) 014503.
[3] E.J. Haug, Computer-Aided Kinematics and Dynamics of Mechanical Systems, vol. I, Prentice-Hall, Englewood Cliffs, New Jersey, 1989.
[4] D.E. Stewart, Rigid-body dynamics with friction and impact, SIAM Rev. 42 (1) (2000) 3–39.
[5] E. Hairer, G. Wanner, Solving Ordinary Differential Equations II: Stiff and Differential-Algebraic Problems, Springer, 1996.
[6] M. Anitescu, Optimization-based simulation of nonsmooth rigid multibody dynamics, Math. Program. 105 (1) (2006) 113–143.
[7] D.P. Bertsekas, Nonlinear Programming, Athena Scientific, Belmont, MA, 1995.
[8] L. Pospisil, Development of Algorithms for Solving Minimizing Problems with Convex Quadratic Function on Special Convex Sets and Applications, Ph.D. thesis, Ostrava Technical University, 2015, http://homel.vsb.cz/~pos220/.
[9] L.E. Malvern, Introduction to the Mechanics of a Continuous Medium, Prentice Hall, 1969.
[10] M.E. Gurtin, E. Fried, L. Anand, The Mechanics and Thermodynamics of Continua, Cambridge University Press, 2010.
[11] R.A. Gingold, J.J. Monaghan, Smoothed particle hydrodynamics: theory and application to non-spherical stars, Mon. Not. R. Astron. Soc. 181 (1) (1977) 375–389.
[12] L.B. Lucy, A numerical approach to the testing of the fission hypothesis, Astron. J. 82 (1977) 1013–1024.
[13] J. Swegle, D. Hicks, S. Attaway, Smoothed particle hydrodynamics stability analysis, J. Comput. Phys. 116 (1) (1995) 123–134.
[14] J.J. Monaghan, Smoothed particle hydrodynamics, Rep. Prog. Phys. 68 (1) (2005) 1703–1759.
[15] A. Colagrossi, M. Landrini, Numerical simulation of interfacial flows by smoothed particle hydrodynamics, J. Comput. Phys. 191 (2) (2003) 448–475.
[16] R.A. Gingold, J.J. Monaghan, Kernel estimates as a basis for general particle methods in hydrodynamics, J. Comput. Phys. 46 (3) (1982) 429–453.
[17] J.P. Morris, P.J. Fox, Y. Zhu, Modeling low Reynolds number incompressible flows using SPH, J. Comput. Phys. 136 (1) (1997) 214–226.
[18] E. Hairer, S. Norsett, G. Wanner, Solving Ordinary Differential Equations I: Nonstiff Problems, Springer, Berlin, 2009.
[19] J.J. Monaghan, On the problem of penetration in particle methods, J. Comput. Phys. 82 (1) (1989) 1–15.
[20] M. Basa, N. Quinlan, M. Lastiwka, Robustness and accuracy of SPH formulations for viscous flow, Int. J. Numer. Methods Fluids 60 (10) (2009) 1127–1148.
[21] S. Adami, X. Hu, N. Adams, A generalized wall boundary condition for smoothed particle hydrodynamics, J. Comput. Phys. 231 (21) (2012) 7057–7075.
[22] W. Hu, Q. Tian, H. Hu, Dynamic simulation of liquid-filled flexible multibody systems via absolute nodal coordinate formulation and SPH method, Nonlinear Dyn. (2013) 1–19.
[23] S. Shao, E. Lo, Incompressible SPH method for simulating Newtonian and non-Newtonian flows with a free surface, Adv. Water Resour. 26 (July 2003) 787–800.
[24] E. Lee, C. Moulinec, R. Xu, D. Violeau, D. Laurence, P. Stansby, Comparisons of weakly compressible and truly incompressible algorithms for the SPH mesh free particle method, J. Comput. Phys. 227 (18) (2008) 8417–8436.
[25] A. Pazouki, D. Negrut, A numerical study of the effect of particle properties on the radial distribution of suspensions in pipe flow, Comput. Fluids 108 (2015) 1–12.
[26] A. Pazouki, R. Serban, D. Negrut, A Lagrangian–Lagrangian framework for the simulation of rigid and deformable bodies in fluid, in: Z. Terze (Ed.), Multibody Dynamics, in: Comput. Methods Appl. Sci., vol. 35, Springer, 2014, pp. 33–52.
[27] A. Pazouki, B. Song, D. Negrut, Boundary Condition Enforcing Methods for Smoothed Particle Hydrodynamics, Tech. Rep. TR-2015-08, Simulation-Based Engineering Laboratory, University of Wisconsin-Madison, 2015, http://sbel.wisc.edu/documents/TR-2015-08.pdf.
[28] A.J. Chorin, Numerical solution of the Navier–Stokes equations, Math. Comput. 22 (104) (1968) 745–762.
[29] S. Cummins, M. Rudman, An SPH projection method, J. Comput. Phys. 152 (2) (1999) 584–607.
[30] X. Hu, N. Adams, A constant-density approach for incompressible multi-phase SPH, J. Comput. Phys. 228 (6) (2009) 2082–2091.

[31] S.M. Hosseini, J.J. Feng, Pressure boundary conditions for computing incompressible flows with SPH, J. Comput. Phys. 230 (19) (2011) 7473–7487.

[32] J. Pozorski, A. Wawreńczuk, SPH computation of incompressible viscous flows, J. Theor. Appl. Mech. 40 (4) (2002) 917–937.

[33] X.Y. Hu, N.A. Adams, An incompressible multi-phase SPH method, J. Comput. Phys. 227 (2007) 264–278, Nov 10.

[34] N. Trask, M. Maxey, K. Kim, M. Perego, M.L. Parks, K. Yang, J. Xu, A scalable consistent second-order SPH solver for unsteady low Reynolds number flows, Comput. Methods Appl. Mech. Eng. 289 (2015) 155–178.

[35] M. Ellero, M. Serrano, P. Español, Incompressible smoothed particle hydrodynamics, J. Comput. Phys. 226 (October 2007) 1731–1752.

[36] K. Bodin, C. Lacoursiere, M. Servin, Constraint fluids, IEEE Trans. Vis. Comput. Graph. 18 (3) (2012) 516–526.

[37] M. Macklin, M. Müller, Position based fluids, ACM Trans. Graph. 32 (July 2013) 104, 12 pp.

[38] S. Marrone, A. Colagrossi, M. Antuono, G. Colicchio, G. Graziani, An accurate SPH modeling of viscous flows around bodies at low and moderate Reynolds numbers, J. Comput. Phys. 245 (2013) 456–475.

[39] P.W. Randles, L.D. Libersky, Smoothed particle hydrodynamics: some recent improvements and applications, Comput. Methods Appl. Mech. Eng. 139 (1–4) (1996) 375–408.

[40] J. Baumgarte, Stabilization of constraints and integrals of motion in dynamical systems, Comput. Methods Appl. Mech. Eng. 1 (1972) 1–16.

[41] H. Mazhar, T. Heyn, A. Tasora, D. Negrut, Using Nesterov's method to accelerate multibody dynamics with friction and contact, ACM Trans. Graph. 34 (3) (2015) 32, 14 pp.

[42] T. Heyn, M. Anitescu, A. Tasora, D. Negrut, Using Krylov subspace and spectral methods for solving complementarity problems in many-body contact dynamics simulation, Int. J. Numer. Methods Eng. 95 (7) (2013) 541–561.

[43] Project Chrono, Chrono: an open source framework for the physics-based simulation of dynamic systems, http://projectchrono.org (Accessed 7 March 2016).

[44] A. Tasora, R. Serban, H. Mazhar, A. Pazouki, D. Melanz, J. Fleischmann, M. Taylor, H. Sugiyama, D. Negrut, CHRONO: an open source multi-physics dynamics engine, in: T. Kozubek (Ed.), High Performance Computing in Science and Engineering, in: Lecture Notes in Computer Science, Springer, 2016, pp. 19–49.

[45] G. Snethen, Xenocollide: complex collision made simple, in: S. Jacobs (Ed.), Game Programming Gems 7, Charles River Media, 2008, pp. 165–178.

[46] G. Snethen, Xenocollide website, http://www.xenocollide.com, September 2007.

[47] H. Mazhar, T. Heyn, D. Negrut, A scalable parallel method for large collision detection problems, Multibody Syst. Dyn. 26 (2011) 37–55, https://doi.org/10.1007/s11044-011-9246-y.

[48] OpenMP, Specification Standard 4.5, Available online at http://openmp.org/wp/, 2017.

[49] K. Iglberger, G. Hager, J. Treibig, U. Rude, High performance smart expression template math libraries, in: International Conference on High Performance Computing and Simulation (HPCS), July 2012, 2012, pp. 367–373.

[50] Y. Nesterov, A method of solving a convex programming problem with convergence rate $\mathcal{O}(1/k^2)$, Sov. Math. Dokl. 27 (2) (1983) 372–376.

[51] A.J. Crespo, J.M. Domínguez, B.D. Rogers, M. Gómez-Gesteira, S. Longshaw, R. Canelas, R. Vacondio, A. Barreiro, O. García-Feal, DualSPHysics: open-source parallel CFD solver based on smoothed particle hydrodynamics (SPH), Comput. Phys. Commun. 187 (2015) 204–216.

[52] J.C. Martin, W.J. Moyce, Part IV. An experimental study of the collapse of liquid columns on a rigid horizontal plane, Philos. Trans. R. Soc., Math. Phys. Eng. Sci. 244 (Mar 1952) 312–324.

[53] F.T. Dodge, The New "Dynamic Behavior of Liquids in Moving Containers", Southwest Research Inst., San Antonio, TX, 2000.

[54] R. Serban, M. Taylor, D. Negrut, A. Tasora, Chrono::Vehicle Template-Based Ground Vehicle Modeling and Simulation, Technical Report TR-2016-10, Simulation-Based Engineering Laboratory, University of Wisconsin-Madison, 2016, http://sbel.wisc.edu/documents/TR-2016-10.pdf.

[55] H. Mazhar, R. Serban, D. Negrut, Using Chrono::FSI and Chrono::Vehicle for the Analysis of Sloshing Phenomena in Vehicle Dynamics Maneuvers, Tech. Rep. TR-2017-02, Simulation-Based Engineering Laboratory, University of Wisconsin–Madison, 2017, http://sbel.wisc.edu/documents/TR-2017-02.pdf.

[56] R. Serban, M. Taylor, D. Melanz, D. Negrut, NG-NRMM Phase I Benchmarking: Chrono Tracked Vehicle Simulation Results Summary, Tech. Rep. TR-2016-08, Simulation-Based Engineering Laboratory, University of Wisconsin–Madison, 2016, http://sbel.wisc.edu/documents/TR-2016-08.pdf.

[57] Simulation-Based Engineering Lab SBEL, Movies, Physics-Based Modeling and Simulation, http://sbel.wisc.edu/Animations (Accessed 9 June 2015).